One-way coupled OpenGGCM/RCM simulation of the 23 March 2007 substorm event

B. Hu,[1] F. R. Toffoletto,[1] R. A. Wolf,[1] S. Sazykin,[1] J. Raeder,[2] D. Larson,[2] and A. Vapirev[2]

[1]   We present results of a simulation of a substorm on 23 March 2007 using the one-way coupled Open Geospace General Circulation Model–Rice Convection Model (OpenGGCM/RCM). In the standalone RCM, inputs are typically taken from empirical models or inferred from satellite data; however, in this simulation, the OpenGGCM magnetic field and plasma information are used to supply inputs and boundary conditions for the RCM. The OpenGGCM ionospheric potential is used to drive a RCM run. That simulation is used to investigate the short time scale dynamics that occurred around substorm onset and assumes the OpenGGCM has a realistic representation of the inner magnetospheric magnetic field during this event. In these runs, a channel of low total entropy plasma opened up on the RCM tailward boundary around substorm onset, and plasma bubbles were injected into the inner magnetosphere. These bubbles were produced by nonadiabatic processes in the OpenGGCM such as magnetic reconnection. We compare the RCM energetic particle flux with measurements from two Los Alamos National Laboratory (LANL) satellites. A dispersionless electron injection is reproduced at the LANL-89 location and a dispersed flux increase at the LANL-97A location. The results indicate the low-$PV^{5/3}$ plasma accompanying magnetic field dipolarization produced earthward plasma motion as the result of these low-entropy flux tubes interchanging their way into the inner magnetosphere; this process may play an important role in substorm particle injection. A comparison simulation in which the electric field is solved by the RCM is also presented, suggesting the need to use RCM's electric field for more accurate inner magnetosphere modeling.

1. Introduction

[2] Improving global magnetohydrodynamics (MHD) models by adding missing physics to particular regions of the magnetosphere has been a longstanding goal in magnetospheric modeling [e.g., *Raeder*, 2003; *Raeder et al.*, 2006; *Lyon et al.*, 2004; *Tóth et al.* 2005, 2007]. In the inner magnetosphere, energy-dependent gradient and curvature drifts are important [*Wolf*, 1983] but are not represented in the MHD transport equations, and efforts have been underway for several years to couple global MHD models to various inner magnetosphere models [e.g., *Toffoletto et al.*, 2003; *Fok et al.*, 2001; *Jordanova et al.*, 2001; *Liemohn et al.*, 1999]. Such coupled models are expected to give a more accurate representation of ring current dynamics and the associated coupling to the ionosphere. Inner magnetosphere models, such as the Rice Convection Model (RCM), require certain inputs such as the magnetic field and plasma boundary condition. By coupling to a global MHD model, the RCM inputs can be self-consistently computed. *De Zeeuw et al.* [2004] presented results from a coupling effort between BATS-R-U.S. (Block Adaptive Tree Solar wind Roe-type Upwind Scheme) [*Powell et al.*, 1999] global MHD code and the RCM, in which a two-way coupled BATS-R-U.S./RCM (where the RCM feeds back pressure) showed some encouraging improvements in the MHD code results, including more pronounced and well defined region-2 currents and more realistic inner magnetosphere pressure. *Toffoletto et al.* [2004] presented first results from the LFM-RCM (Lyon-Fedder-Mobarry) [*Lyon et al.*, 2004] and showed that one-way coupling produced more realistic region-2 currents and ring current-ion pressures in the RCM. More recently, *Fok et al.* [2006] used LFM results of a substorm simulation as input to the CRCM (Comprehensive Ring Current Model) [*Fok et al.*, 2001] and reproduced observable features of oxygen enhancement during a substorm. *Moore et al.* [2008] studied

---

[1]Department of Physics and Astronomy, Rice University, Houston, Texas, USA.
[2]Space Science Center, University of New Hampshire, Durham, New Hampshire, USA.

the effect of a plasmaspheric plume using results from one-way coupled LFM and CRCM model. *Buzulukova et al.* [2010] presented one-way coupled BATS-R-U.S. and CRCM model simulations for both an idealized case and an actual storm and showed the model reproduced many known features of the inner magnetosphere dynamics.

[3] The results presented in this paper are from the OpenGGCM-RCM (Open Geospace General Circulation Model) [*Raeder et al.*, 2001] coupling efforts. While the fully coupled OpenGGCM-RCM code, in which the RCM also feeds back both density and pressure to OpenGGCM, is currently undergoing testing, we used the forward coupling mode to simulate a substorm event that occurred on 23 March 2007. Unlike geomagnetic storms, which are the result of many hours or days of strong southward IMF, geomagnetic substorms are shorter processes on a time scale of a few hours. Thus the injection process is expected to be less sensitive to RCM pressure feedback to the OpenGGCM. We chose the 23 March event because it is a well-known THEMIS substorm that has been extensively studied [e.g., *Angelopoulos et al.*, 2008; *Keiling et al.*, 2008a, 2008b; *Liu et al.*, 2009; *Zhu et al.*, 2009] and the standalone OpenGGCM simulation is available for comparison [*Raeder et al.*, 2008].

[4] The standalone OpenGGCM simulation of the 23 March event reasonably well reproduced many substorm salient features including rapid field dipolarization, a westward traveling surge, and an increase in density observed by some THEMIS probes [*Raeder et al.*, 2008]. The magnetic field produced by the model also shows good agreement with THEMIS observations. However, since the MHD description is only single fluid, lacking inner magnetosphere energy-dependent drift physics, it can only provide single fluid information about a particle injection, and is not able to capture dispersion features related to energetic particle injection [e.g., *Belian et al.*, 1978; *Mauk and Meng*, 1987; *Thomsen et al.*, 2001]. Injection of high-energy particles into the inner magnetosphere is one of the major indicators of substorm onset. There are already many models that use test particle simulations in either specified electromagnetic pulse or precomputed MHD electric and magnetic field [e.g., *Zaharia et al.*, 2000, 2004; *Birn et al.*, 1997, 1998; *Li et al.*, 1998, 2003; *Liu et al.*, 2009]. *Taktakishvili et al.* [2007] did metrics analysis on two proton injection events using the Fok ring current model [*Fok et al.*, 1999] driven by precomputed magnetic/electric field and plasma information from the BATS-R-U.S. MHD model, and found the model performed fairly well for the injection event under strongly varying solar wind conditions. *Zhang et al.* [2007] did a storm simulation using two-way coupled BATS-R-U.S./RCM; they compared the model outputs to geosynchronous plasma moments data and they found good agreement. Our initial assumption in this work was that the OpenGGCM reasonably well represents the magnetic field during the substorm. Since the effect of the induced electric field is implicitly included through time-dependent magnetic field mapping [*Toffoletto et al.*, 2003], the coupled OpenGGCM-RCM model is a self-contained tool to cover the injection part of the substorm simulation.

[5] Recent work using the RCM to simulate substorm injections has shown the consistency of the picture that these injections are associated with earthward moving magnetic bubbles. A bubble is defined as a set of magnetic flux tubes in the magnetosphere that have a lower-entropy parameter $PV^{5/3}$ than their surroundings [e.g., *Pontius and Wolf*, 1990; *Birn et al.*, 2004; *Zhang et al.*, 2008; *Wolf et al.*, 2009], where P is the plasma pressure and $V = \int_s^n dS/B$ (B is the magnetic field strength and the integral is along the magnetic field line, from the southern hemisphere to the northern hemisphere) is the flux tube volume. It is believed that these bubbles are produced by an nonadiabatic process such as magnetic reconnection [*Birn et al.*, 2006] or current disruption in the inner part of the plasma sheet [e.g., *Lui et al.*, 1992; *Sitnov et al.*, 2007; *Wolf et al.*, 2009] and they are important for plasma transport from tail to inner magnetosphere [e.g., *Lyons et al.*, 2003; *Apatenkov et al.*, 2007; *Sergeev et al.*, 1996]. Observational evidence of a bubble propagation in the inner magnetosphere has emerged from Cluster and Double Star observations [e.g., *Walsh et al.*, 2009], which support the existence of an earthward moving bubble as near as 7 R_E. Recent modeling work has also suggested that these bubbles play a crucial role in the injection of plasma into the stormtime ring current. Using a self-consistent RCM-E simulation, where the magnetic field is computed to be in force equilibrium with the RCM-computed plasma pressures, *Lemon et al.* [2004] showed that even under strong convection, plasma cannot be injected into the inner magnetosphere, unless one reduces $PV^{5/3}$ below typical middle-plasma sheet values. *Yang et al.* [2008] simulated a saw-tooth event using the RCM, by treating each tooth as separate substorm and manually reducing the $PV^{5/3}$ on the RCM boundary at each expansion phase with the intentional goal of matching observations. The simulated energetic particle flux and neutral atom fluxes matched well with observations. *Zhang et al.* [2008, 2009] presented another RCM simulation that injects a bubble into the inner magnetosphere, also by performing a reduction of $PV^{5/3}$ over a range of local time at the RCM simulation boundary, and correspondingly increasing the electric field E_y. In either of the above simulations, a bubble is introduced through the RCM outer boundary assuming that the bubble is produced by a process outside the RCM modeling region. Thus, a RCM or RCM-E simulation of a substorm always involves a depletion of $PV^{5/3}$ on the boundary resulting in the injection of the bubble. In this study, when the substorm produces bubbles in the MHD model, they propagate into the inner magnetosphere via interchange [*Wolf et al.*, 2009].

[6] In this study, we use the one-way coupled OpenGGCM-RCM model to study the injection event in the 23 March 2007 substorm and compare model results with data from different LANL geosynchronous satellites. We explore the features of the bubble that was injected into the inner magnetosphere during the substorm expansion phase and discuss the creation of the bubble. In the initial run, we used the ionospheric potential distribution computed by OpenGGCM to compute the ionospheric potential distribution that transports particles in the RCM. We will label this run RCM Run1 or Run1 in this paper. We also present a comparison run that uses the ionospheric electric field computed from RCM pressures and Birkeland currents. This run will be labeled as RCM Run2 or Run2. The first part of the paper will describe in detail the model setup and coupling methodology. In the second part, we show model results of the substorm event including comparisons with observations. In the latter part of the paper, we explore how the bubbles are

created in the MHD simulation and also discuss features of the self-consistent electric field. Section 5 gives conclusions and summarizes the paper. Appendix A describes the equations used in the information exchange in the code coupling.

2. Model Description and Setup

2.1. OpenGGCM Description

[7] The OpenGGCM is a large-scale model of the Earth's magnetosphere originally developed at UCLA by Raeder [*Raeder et al.*, 1998]. The OpenGGCM self-consistently solves the MHD equations for the magnetic field, plasma density and pressure and ionosphere potential in its simulation domain. The current version of OpenGGCM consists of three components: the global magnetosphere, the ionosphere and the CTIM (Coupled Thermosphere Ionosphere Model) [*Fuller-Rowell et al.*, 1996; *Raeder et al.*, 2001] module. The global magnetosphere model solves the semiconservative MHD equations inside the simulation domain to the inner boundary which is at about 3.5 R_E. The OpenGGCM uses a stretched-Cartesian grid which not only allows straightforward and efficient parallelization, but also has optimized grid resolution near regions of interests. For spatial discretization, the OpenGGCM uses a hybrid flux construct scheme (switch between a fourth-order and a first-order Rusanov flux scheme, depending on the gradients in the solution.) and an explicit predictor-corrector finite difference scheme in time stepping. It is important in every MHD model that the divergence of magnetic field is kept close to zero and the OpenGGCM achieves this by putting variables on a staggered grid, which can maintain zero divergence to numerical roundoff [*Evans and Hawley*, 1988]. The code uses an anomalous resistivity which is parameterized by the local current density, and is nonzero only when the current density exceeds a specified threshold. Birkeland currents at the inner boundary are mapped to the ionosphere assuming a dipole magnetic field; these currents are used to solve for the potential in the ionosphere using $\nabla \cdot \Sigma \cdot \nabla \Phi = -j_\parallel \sin I$ where I is the field inclination angle at the ionosphere and Σ is the conductance tensor. The potential is then mapped back to the inner boundary of the MHD code which is used as a boundary condition. The ionospheric component of the model is coupled to the CTIM model, which takes inputs from the MHD model for electron precipitation parameters and electric field. It also uses parameterized solar 10.7 cm flux and the tidal modes. CTIM self-consistently solves the neutral and ion fluid equations to provide conductances to the OpenGGCM ionosphere for the potential calculation. A detailed description of the OpenGGCM can be found in the works by *Raeder* [2003] and *Raeder et al.* [2008].

2.2. Rice Convection Model

[8] The Rice Convection Model (RCM) is an inner magnetosphere model that has been developed at Rice University [e.g., *Wolf*, 1970; *Jaggi and Wolf*, 1973; *Harel et al.*, 1981; *Wolf*, 1983; *Spiro et al.*, 1988] and is designed to carefully treat the physics of the inner magnetosphere and its coupling to the ionosphere using a scheme first proposed by *Vasyliunas* [1970]. By neglecting the inertial terms in the MHD momentum equation and assuming a known time-dependent magnetic field, the RCM computes bounce-averaged particle motion in the slow flow region of the inner magnetosphere on a 2 dimensional ionospheric grid. The RCM assumes an isotropic pitch angle distribution and treats different energy components in the plasma distribution function as independent fluids (channels), each with an energy invariant λ_s. Using adiabatic drift convection theory, the kinetic energy for given plasma fluid with energy invariant λ_s and location x is given by $W(\lambda_s, x, t) = \lambda_s V^{-2/3}$. The RCM computes currents, electric field and particle $\vec{E} \times \vec{B}$ and gradient-curvature drifts of each channel self-consistently, given user specified plasma distribution and potential on the boundary. The basic equations used in RCM for the plasma evolution are

$$\left(\frac{\partial}{\partial t} + \vec{v}_s \cdot \nabla\right)\eta_s = S(\eta_s) - L(\eta_s), \tag{1}$$

$$\vec{v}_s = \frac{\lambda_s}{q_s B^2}\vec{B} \times \nabla V^{-2/3} + \frac{\vec{E} \times \vec{B}}{B^2}, \tag{2}$$

and

$$\vec{E} = -\nabla(\Phi_{iono} + \Phi_{corotation}), \tag{3}$$

where $\vec{v}_s$ is the bounce-averaged particle drift velocity for channel s, η_s is the number of particles per unit magnetic flux(flux tube content), q_s is the particle charge, S and L are the sources and losses and $\vec{E}$, $\vec{B}$ have their usual meaning as electric and magnetic field, respectively. The induction E-field is introduced by time varying magnetic field mapping from the ionosphere. The RCM has its own routines for calculating Birkeland currents as well as ionospheric conductances and potentials, but in the coupled code, Φ_{iono} can come either from the OpenGGCM (for RCM Run1) or the RCM (for RCM Run2. A more detailed description of the RCM can be found in the review paper by *Toffoletto et al.* [2003 and references therein].

2.3. Coupling Methodology

[9] As noted in sections 2.1 and 2.2, the RCM and OpenGGCM work on different spatial domains and use different mathematical descriptions and coordinate systems. In order to couple the two codes, conversion of three-dimensional plasma moments to field-line averaged values and back is required. Figure 1 shows the diagram of the coupling methodology. Since the RCM operates only in the closed field line region, field lines are traced to find the open/closed boundary and MHD-based plasma information is averaged along the field line (see Appendix A). At each exchange time (every 1 ~ 5 min, 3 min used in this paper), the MHD nodes assemble the necessary field and plasma information and send it to the RCM. The OpenGGCM ionosphere node also assembles the potential (without corotation), and when needed, the conductance information and sends them to the RCM. The RCM node then uses this information to prepare a run for the RCM, tracing from every RCM ionosphere grid point to get the field mapping information and flux tube volume, as well as the field-line-averaged temperature and density on the polar boundary. Coordinate transformations are conducted in the tracing to convert the MHD information, which is in GSE coordinates, to the RCM, which works in SM coordinates. (The standalone RCM can be thought to be working in GSM coordinates, though, since GSM and SM are
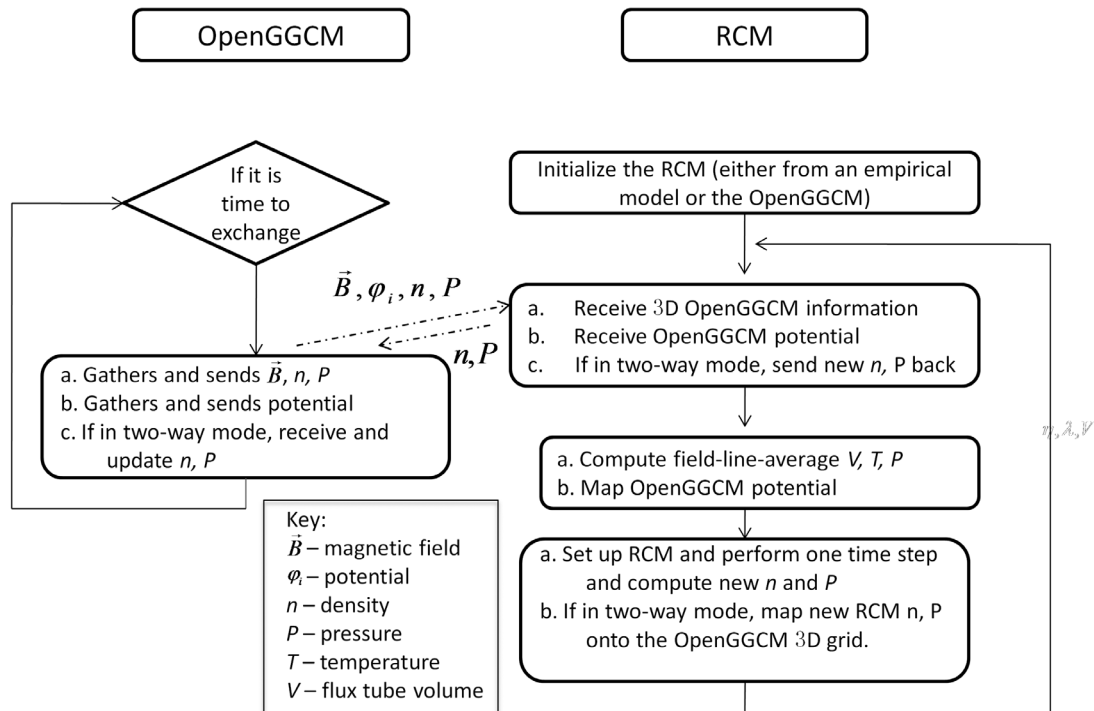
Figure 1. Diagram of OpenGGCM and RCM coupling methodology for the case where the RCM uses the ionospheric potential computed by OpenGGCM.

the same within the assumption of a zero dipole tilt). The RCM assumes symmetry between the two hemispheres and its grid is in the northern hemisphere. For simplicity, only the potential and conductance (for RCM Run2) on the OpenGGCM northern ionosphere are mapped onto the RCM grid, and the corotation potential is included in the RCM calculations. For MHD runs with nonzero dipole tilt, the ionospheric potential is not necessarily the same at the ionospheric footprints of a field line, due to numerical errors in the MHD code, and that causes errors in the coupled-code results. Figure 2 indicates the size of this error, by comparing the MHD-computed potential drop across the RCM modeling region for the two hemispheres; we find they differ by less than 20%. Due to the nonzero dipole tilt, the MHD conductances at the northern and southern ionospheric footprints of a field line may be the different; our use of just the northern-ionospheric conductance is also a source of error in the coupled-code results. Another option would be to use the averages of the MHD potentials for RCM Run1 and the total conductance, total Birkeland current, and average boundary potential for RCM Run2 [e.g., *Buzulukova et al.*, 2010].

[10] When the RCM gets all the necessary information, it creates input files which have the formats that are normally used by the standalone RCM. The coupling interface specifies the start and stop time and calls the main RCM program to run for an exchange interval. When the RCM finishes its calculation, it can use the MHD-based magnetic field to update the pressures and densities at MHD grid points. The OpenGGCM code runs simultaneously when RCM is running, until the next exchange time, at which the MHD nodes will receive updated RCM pressure and density information. The MHD can choose to use this information to nudge its

pressure and density (in this case we call it a two-way coupled run). Since the two-way coupled code is currently undergoing testing, the simulation presented here, in which a high-resolution MHD grid is used, the feedback is turned off, i.e., the MHD code only sends its information to the RCM and there is no feedback to the MHD.

2.4. Model Inputs and Setup

[11] For the results presented here, all MHD parameters are set as in *Raeder et al.* [2008]. The run time for the OpenGGCM and RCM was from 7:00 UT to 15:00 UT on 23 March 2007. The model inputs include the upstream solar wind and interplanetary magnetic field (IMF) which are taken from the WIND satellite at ~198 R_E sunward. The solar wind and IMF are propagated ballistcally to the sunward boundary of the simulation (20.01 R_E) at the prevailing solar wind
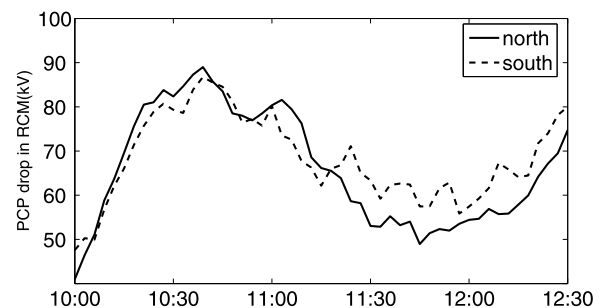
Figure 2. Potential drop (kV) at the RCM polar boundary for the northern (solid line) and southern hemisphere (dashed line).
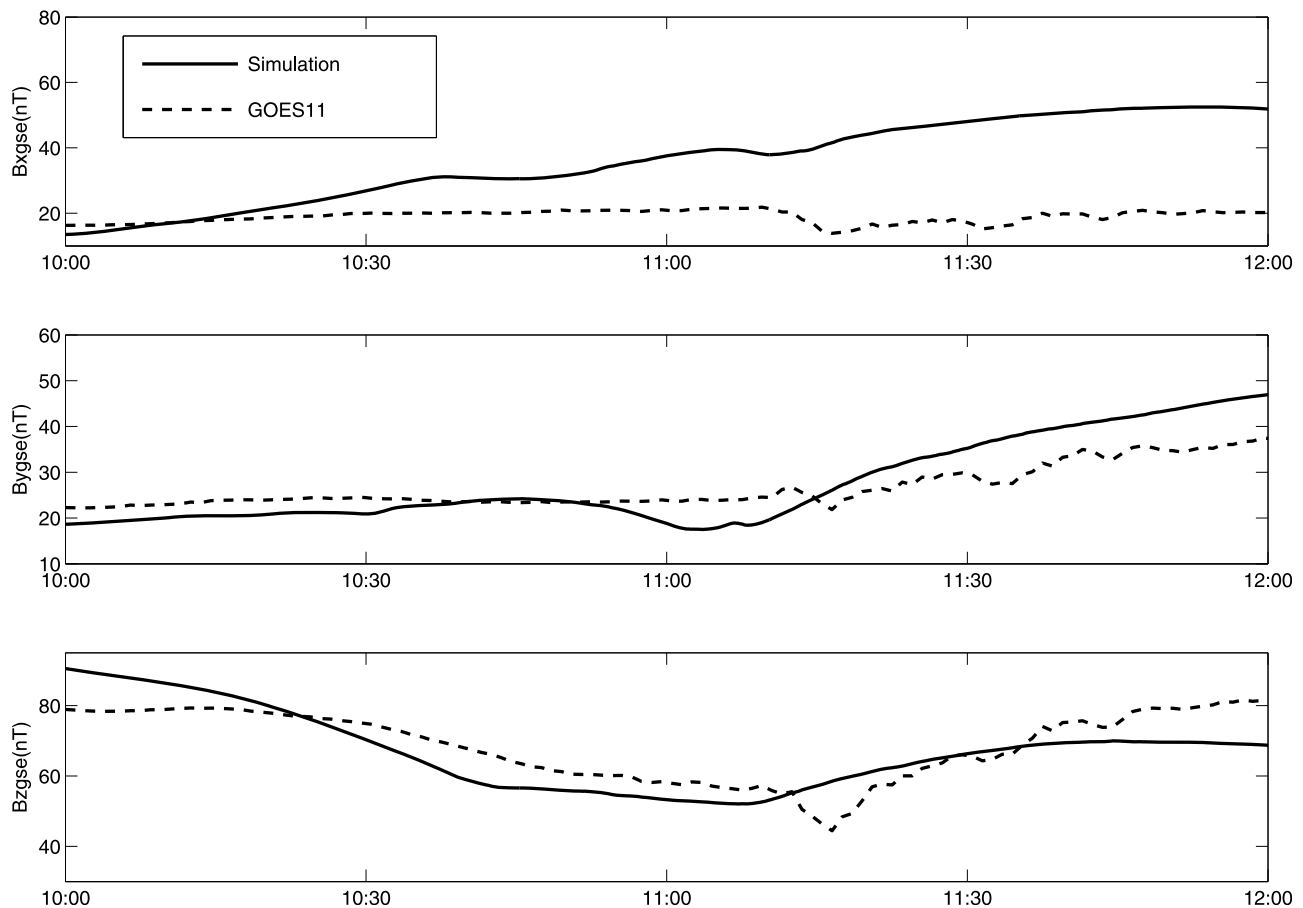
Figure 3. Comparison of magnetic fields measure by GOES11 (dashed line) and OpenGGCM simulation (solid line, not time-shifted) as a function of UT. GOES11 is around 01–02 MLT.

speed. The orientation of the solar wind magnetic structure is taken into account by computing the normal direction of the solar wind discontinuities using the minimum variance method [*Raeder et al.*, 2001]. The coupled thermosphere ionosphere model (CTIM) was used for more realistic conductance calculation. The OpenGGCM grid for this run contains 37.8 million cells and the smallest grid spacing is ~0.15 R_E. The RCM grid resolution in latitude and longitude is 200 × 101. For the RCM calculation, we used 200 invariant energy channels and the *Spence and Kivelson* [1993] model for the initial setup of the plasma distribution. While there is an option to use the MHD plasma information for the RCM's initial condition, but that results in unrealistically low particle fluxes, due the unrealistically low initial particle pressure in the MHD code's inner magnetosphere. We assume a kappa distribution in converting from single fluid quantities to RCM multifluid information, where $\kappa = 5$ was assumed for protons and $\kappa = 3$ is for electrons. These kappa parameters were chosen to be in a reasonable range as discussed by *Yang et al.* [2008] and *Christon et al.* [1988]. The RCM takes magnetic field and boundary information from the OpenGGCM throughout the run except for the initial plasma condition. A comparison of magnetic field between OpenGGCM simulation and measurements by GOES11 (around 01–02 MLT during the injection) is shown in Figure 3. The MHD time in Figure 3 is in simulation UT and has not been time-shifted.

The value Φ_{iono} in equation (3) is taken from OpenGGCM by default but the potential can be also solved by the RCM. We present results from using both ionospheric potentials. All loss mechanisms in RCM (charge exchange for ions and strong pitch angle scattering for electrons) are turned off for simplicity. Charge exchange for the ions is a relatively slow process and would have small effect on the short simulation presented here, but electron losses can be significant. As a result, in both cases the simulation should tend to overestimate particle fluxes, particularly for electrons. The number of channels (~200) and the energy invariant (λ) associated with each channel are preset before the run to ensure that the distribution function is properly resolved at the tailward boundary.

3. Model Outputs and Results for RCM Run1

3.1. Bubbles

[12] It is believed that during the expansion phase of a magnetic substorm, depleted flux tubes in the plasma sheet are formed, possibly because of reconnection or some other nonadiabatic process such as current disruption [*Zhang et al.*, 2008, 2009; *Wolf et al.*, 2009]. These bubbles have a lower $PV^{5/3}$ than their surroundings and are interchange unstable. They tend to move earthward and sometimes are seen as BBFs (Bursty Bulk Flows) in the plasma sheet [e.g.,
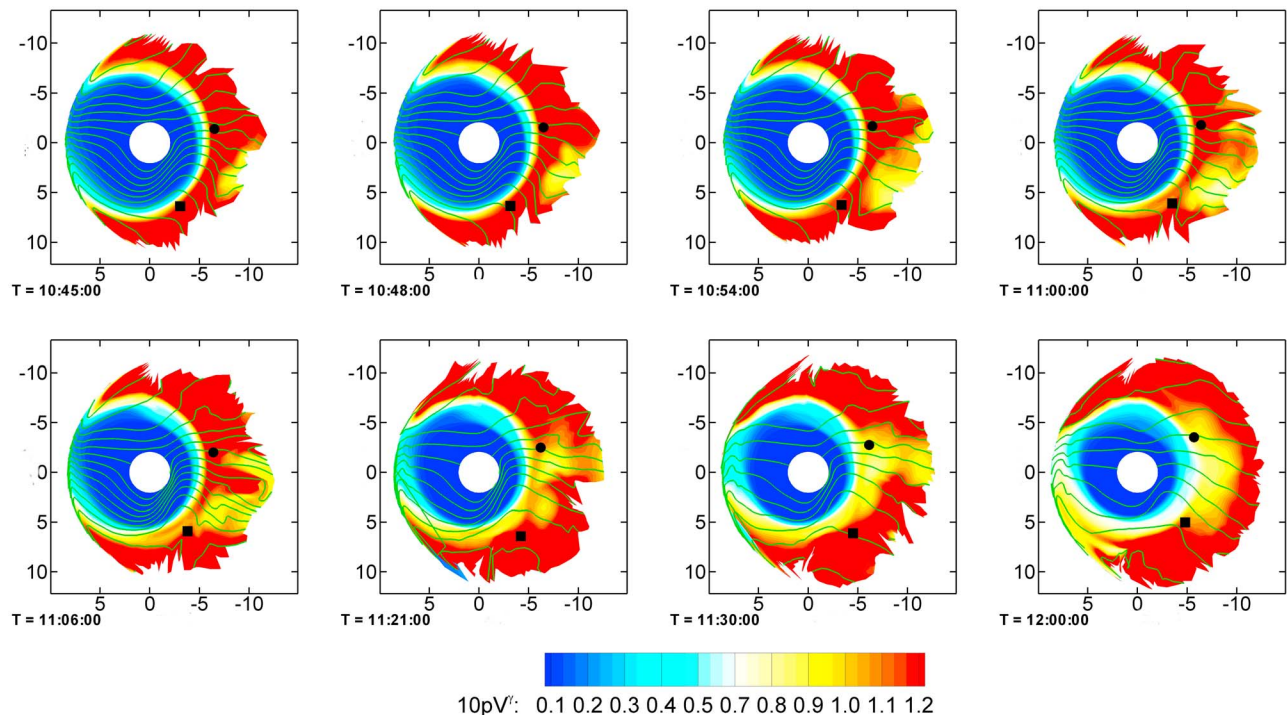
Figure 4. $PV^{5/3}$ [nPa(R_E/nT)$^{5/3}$] time series of the bubble injection on the RCM equatorial plane with potential solved by OpenGGCM (5 kV spacing) for RCM Run1. The Sun is to the left. Locations of LANL97A (LANL89) are marked as squares (circles).

Angelopoulos et al., 1994]. These high-speed flows or bubbles are thought to be one of the major mechanisms for tail flux transport and bringing plasma sheet particles near the Earth during geomagnetically active periods. Figure 4 shows eight RCM equatorial time series snapshots for $PV^{5/3}$[nPa(R_E/nT)$^{5/3}$] from Run1, after the "code substorm onset time" (~10:40 simulation time in the MHD [*Raeder et al.*, 2008]; we will use the simulation time in this paper). The Sun is to the left. The first two plots in Figure 4 show how the low-$PV^{5/3}$ channel (yellow in color) that starts to open up in the midnight sector at simulation time ~10:45 UT. In the subsequent plots, this low-$PV^{5/3}$ channel expands in local time (e.g., centered in the premidnight sector between 2100 LT and 0130 LT as shown in the fourth plot in Figure 4), which is consistent with the conclusion of *Liu et al.* [2009] that the injection initiated between 2100 LT and 0100 LT. The leading edge of the bubble moves closer to the Earth and has a tendency to travel westward because of gradient and curvature drifts. From the time series of the contours, the potential electric field increases in the bubble region during the injection and exhibits weak shielding near the Earth. Throughout the injection, the entropy parameter of the newly injected flux tubes is ~0.06 (nPa(R_E/nT))$^{5/3}$; the bubble reached ~5 R_E from the Earth. There are also signatures of possible interchange instability on the leading edge of the bubble, as seen by the presence of the finger-like structures in the second plot. The closure of this low-$PV^{5/3}$ channel took place at ~11:45 UT; by 12:00 UT, the $PV^{5/3}$ configuration in the inner magnetosphere has almost returned to the pre-injection state.

[13] The equatorial RCM pressure from Run1 before and after the bubble injection is shown in Figures 5a and 5b. The

pressure in the inner magnetosphere increases and the peak pressure occurs closer to Earth after the bubble injection. These features of the model-produced bubble are qualitatively in agreement with the results presented by *Zhang et al.* [2008, 2009] and the picture first suggested by *Pontius and Wolf* [1990]. However, the way that the OpenGGCM imposes low-$PV^{5/3}$ boundary condition seems to be different from *Zhang et al.* [2008] in which the flux tube content is reduced at the boundary, but the magnetic field is not changed correspondingly. In the OpenGGCM run, despite the slight change in particle pressure, the RCM sees rapid magnetic field dipolarization at the boundary starting at ~10:40 (at $x = -9$ R_E, $B_z = 23.9$ nT at 10:45, comparing to $B_z = 13$ nT at 10:36). *Zhang et al.* [2009] include the field stretching and collapsing of the magnetic field. Thus, in the MHD results as well as in the work by *Zhang et al.* [2009], P changes relatively little, and the decrease in $PV^{5/3}$ is mostly associated with the decrease in V during the dipolarization. Figure 5c shows the OpenGGCM pressure in the equatorial plane, and it is much weaker than the RCM computed pressure in Figures 5a and 5b. Examples of OpenGGCM Birkeland currents and RCM computed Birkeland currents (from Run2) are shown in Figures 5d and 5e. The currents from the OpenGGCM are more diffusive and the region-2 currents are weaker. Figure 5f shows higher ion and electron temperature in the injection region for Run1.

3.2. Bubble Creation in the OpenGGCM

[14] To provide a closer look at how these bubbles are created in the MHD code, Figure 6 shows the entropy parameter $PV^{5/3}$ in the equatorial plane in the MHD domain along with the field line shape and the velocity in the
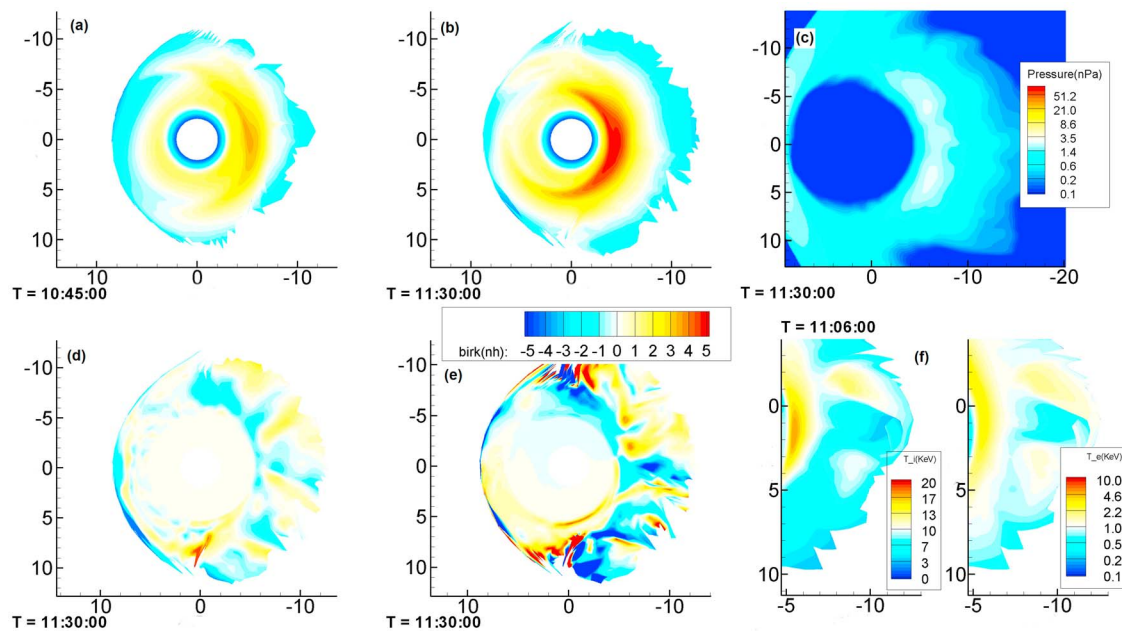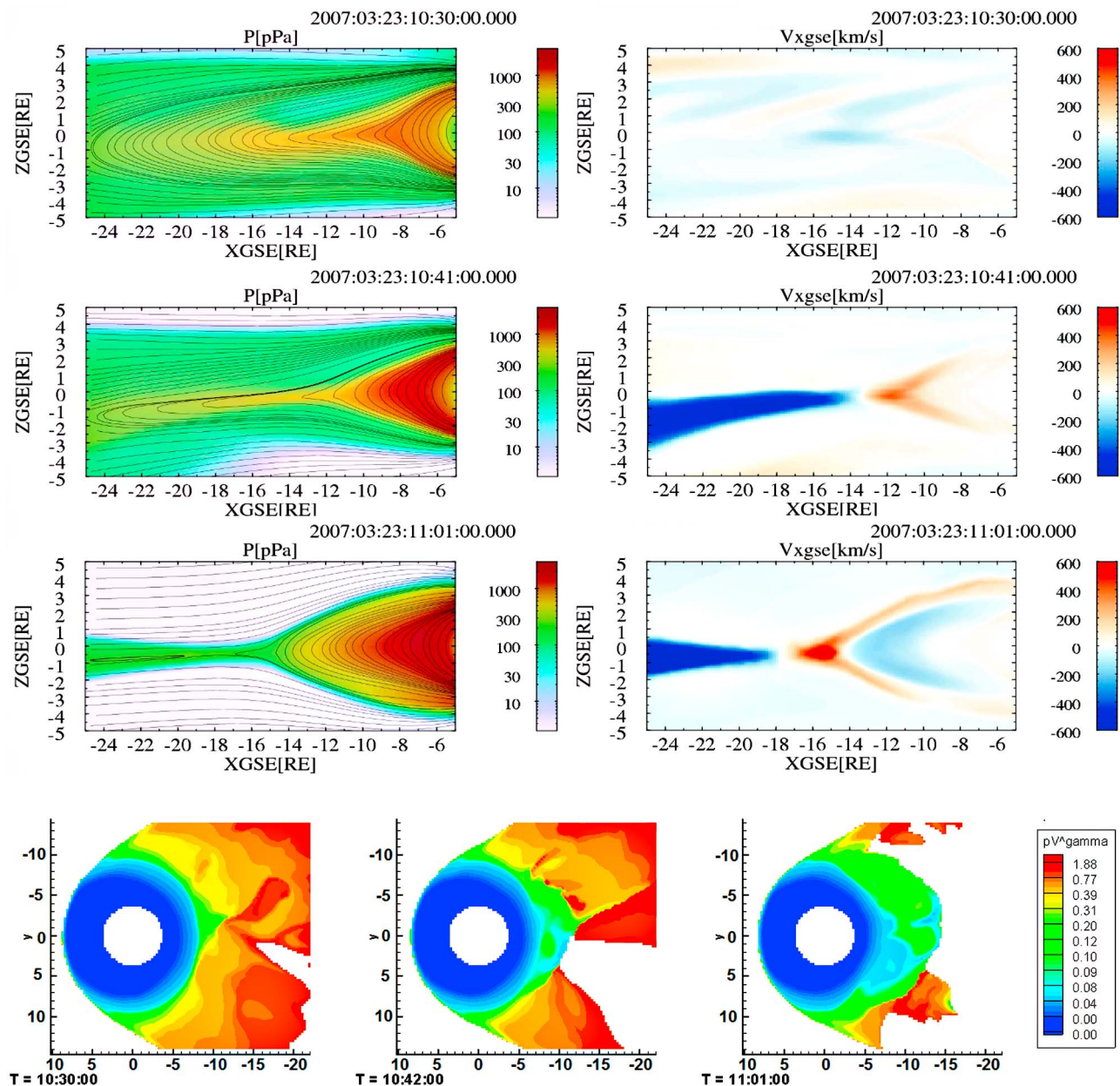
Figure 5. (a and b) RCM pressure on the equatorial plane before and after the onset from Run1. (c) OpenGGCM pressure on the equatorial plane after onset. (d and e) Comparison of equatorial maps of ionospheric Birkeland currents computed by OpenGGCM (Figure 5d) and the RCM from Run2 (Figure 5e). (f) RCM ion and electron temperatures (keV) in the equatorial plane from Run1.

noon-midnight meridian, for three different times: 10:30 UT, 10:42 UT and 11:01 UT. The first three rows are plasma pressure with field lines and flow velocity in x direction in the noon-midnight meridian plane, with the Sun to the right. The last row presents the field line averaged quantity $PV^{5/3} = \left(\int_{s}^{n} P^{3/5} \frac{ds}{B} \right)^{5/3}$, plotted on the magnetic equatorial plane, with the Sun to the left. Since $PV^{5/3}$ is a field line averaged quantity, points not on closed field lines are not shown. The field line tracing was stopped at the $\sim 4\ R_E$ inner shell because inside the inner boundary the MHD field is assumed to be dipolar and is constant with time.

[15] At 10:30 UT, which is near the end of the substorm growth phase, the field lines are quite stretched and there are no noticeable earthward flows. Most of the plasma sheet points are on closed field lines, though there is a patch of open field lines toward the dusk side of midnight; they show up as blank in the equatorial plane. Postmidnight, there is a pair of high-/low-$PV^{5/3}$ flux tubes and we will discuss this in the next paragraph. The MHD code onset time is about 10:42 UT [*Raeder et al.*, 2008], when earthward flows are seen in the $\sim 13\ R_E$ region, associated with the field dipolarization. (Actual substorm onset occurred 30 min later.) A bubble emerges from the reconnection site, which is duskward of the local midnight, and moves earthward at an MHD-estimated speed of ~ 160 km/s. At around the same time, the RCM sees a depleted $PV^{5/3}$ channel opening at its tailward boundary ($\sim 10\ R_E$). The third column of the $PV^{5/3}$ plots shows time 11:01 UT, by which time the reconnection that powers the major activation of the substorm, occurs over a wide range of local times resulting strong earthward and tailward flow. One can also see this from the field topology; the X line is

at $\sim 17\ R_E$ at local midnight. Magnetic field lines are quite dipolarized earthward of the X line, and the current sheet is thinning on the tailward side. The $PV^{5/3}$ plot for 11:01 UT (Figure 6, bottom right) shows that depleted flux tubes are formed and bubbles rapidly move earthward with an MHD-estimated speed of ~ 200 km/s. These bubbles are emerging from the X line and they gradually slow down as they travel closer to the Earth into the RCM modeling region. In fact, reconnection at $\sim 20\ R_E$, which results in consistent earthward flows, lasts until $\sim 11{:}30$; during the expansion phase, the reconnection site moves more tailward.

[16] In the substorm growth phase ($\sim 10{:}22$), at $\sim 11\ R_E$ toward the dawn side of local midnight, a local maximum in $PV^{5/3}$ (blob) appears next to a minimum in $PV^{5/3}$ (bubble), Figure 7 shows the $PV^{5/3}$ on the equatorial plane and the OpenGGCM flow velocity in x direction, for UT 10:22, 10:25 and 10:28. The anomalous resistivity as computed by the OpenGGCM is shown as black spots in the $PV^{5/3}$ plots (Figure 7, top) with the Sun to the left. From left, the blob is seen at $\sim 10{:}22$; it moves antisunward and is associated with patches of anomalous resistivity. The anomalous resistivity is determined by local current and it must reach certain threshold before switched on thus it is nonzero for only a few grid points in strong current sheets [*Raeder et al.*, 1998]. From the results, the blob forms while the anomalous resistivity is zero, so its formation is possibly due to numerical resistivity. The OpenGGCM flow plots in Figure 7 (bottom) show both the earthward flow of the bubble and the anti-sunward motion of the blob, which accelerates as it travels tailward. This weak bubble moves earthward but it does not propagate deep into the inner magnetosphere. The separation of the bubble and the blob could create a more favorable

Figure 6. (top) The three rows show midnight-meridian plane cut for OpenGGCM pressure with magnetic field line topology and velocity in GSE x direction with the Sun to the right. (bottom) $PV^{5/3}$ on the equatorial plane with the Sun to the left (there are no $PV^{5/3}$ values in the white region due to field line traces not being closed). The three frames are for (left) 10:30, (middle) 10:42, and (right) 11:01 UT.

magnetospheric configuration for further instabilities such as magnetic reconnection to occur. Thus, the interchange instability resulted from the bubble/blob pair may have important implications for the substorm expansion phase, though careful further study is needed to confirm this simulation result.

[17] Overall, the majority of bubbles that propagate into the RCM modeling region during the substorm expansion phase are caused by magnetic reconnection in the tail which powers the main activation of the substorm. There are multiple reconnection sites during this event and bubbles created at different locations tend to have different properties. The field is quite dynamic during the substorm expansion phase and more investigations are needed to fully understand the onset mechanism in this event.

3.3. LANL Energetic Particle Flux and MPA Measurements

[18] In this section, we compare our model produced particle flux with two LANL satellites LANL89-046 and LANL97A at geosynchronous orbit, where an increase in high-energy particle flux is often observed during a substorm expansion phase. The energization of these particles is often attributed to induced, impulsive electric fields possibly associated with field dipolarization. There is evidence that
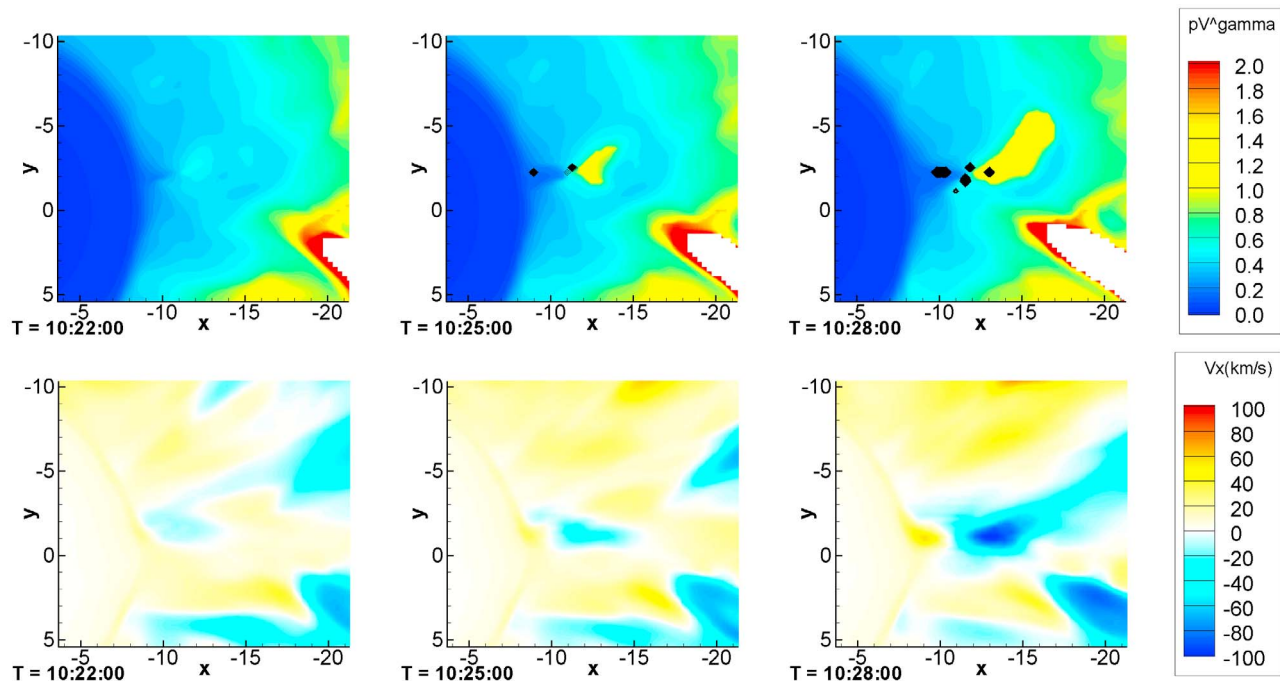
Figure 7. (top) $PV^{5/3}$ and (bottom) OpenGGCM flow velocity in GSE x direction on the RCM equatorial plane, for (left) 10:22, (middle) 10:25, and (right) 10:28 UT. The black spots on $PV^{5/3}$ plots indicate where the anomalous resistivity in the OpenGGCM is nonzero.
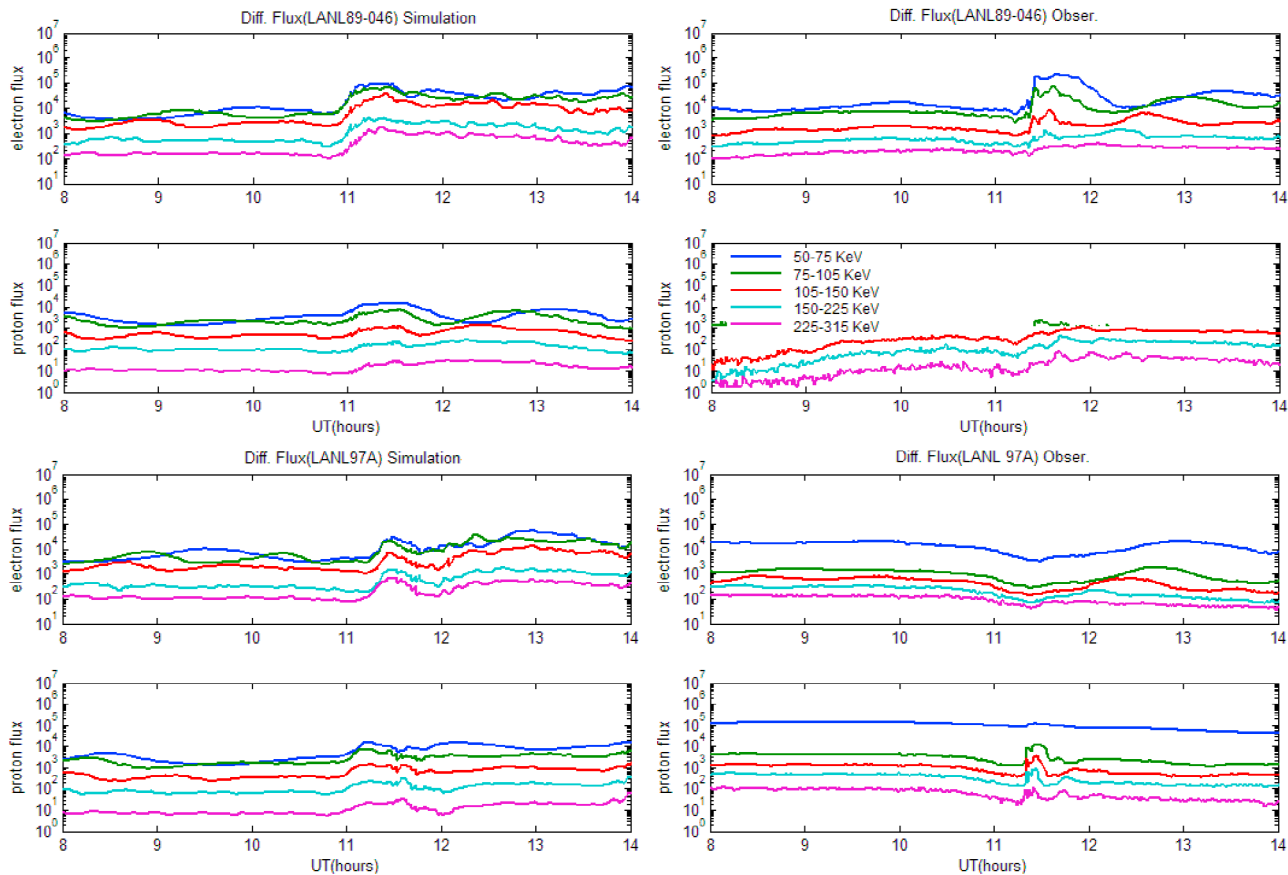
Figure 8. (left) Simulated SOPA fluxes versus (right) observations for satellite LANL89-064 and LANL97A for RCM Run1. The energies are 50–75, 75–105, 105–150, 150–225, and 225–315 keV, from blue to purple. The simulation results have been time-shifted 30 min.
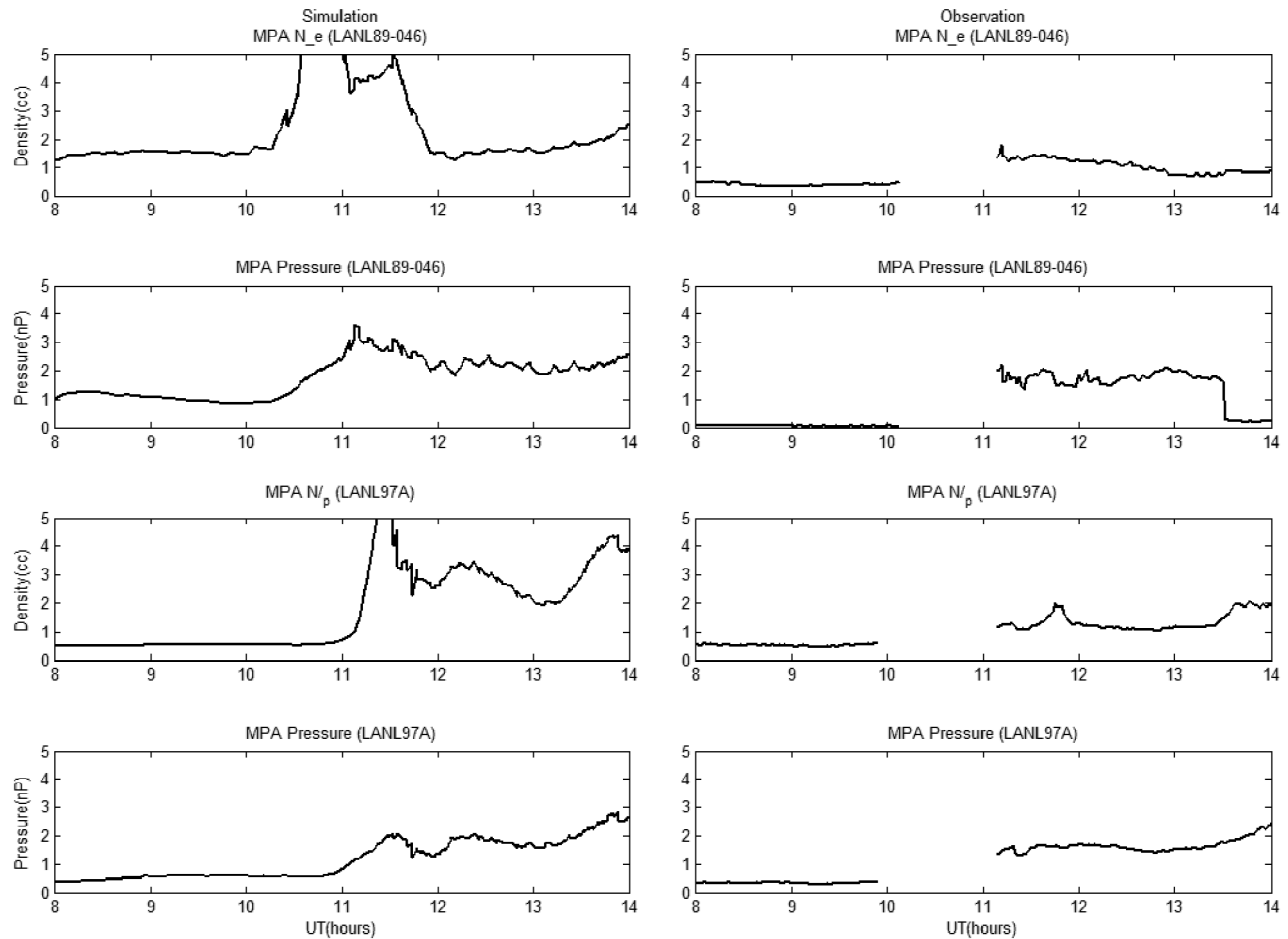
Figure 9. Top four plots are MPA moments for (left) simulation versus (right) observations for satellite LANL89-064 from RCM Run1. Bottom four plots show MPA moments for simulation versus observations for satellite LANL97A from RCM Run1. The simulation results have been time-shifted 30 min.

earthward moving bubbles are also associated with a substorm injection [e.g., *Lyons et al.*, 2003].

[19] At substorm onset, LANL89-046 satellite was located near local midnight and LANL97A near 2100 LT. Figure 8 shows comparisons for RCM Run1 between the energetic particle differential flux ($/cm^2/s/sr/keV$) measured by SOPA instruments on LANL89-046 and LANL97A and the simulation outputs. Since the OpenGGCM onset time is ~10:40 UT, earlier than the actual onset times (~11:00 UT and 11:19 UT), we time-shifted the simulation 30 min for easier comparison with observations. The discrepancy in onset time may be due to the preconditioning in the MHD code. In this run, the MHD code started 4 h before the actual event which may not be long enough to remove any remnants of the initial condition used to start the MHD code [*Raeder et al.*, 2008]. Other effects such as insufficient resolution in the MHD code, and missing physics such as kinetic effects and feedback from an inner magnetosphere model such as the RCM may also play a role in the timing of substorm onset. For the post midnight satellite LANL89-046, a major dispersionless electron injection is observed along with an increase in proton fluxes that exhibits a slight dispersion. The simulation results for LANL89-046 basically reproduce the dispersionless elec-

tron injection, and the ion flux is also roughly in agreement with observations.

[20] For the premidnight satellite LANL97A, an ion injection with small dispersion is observed and this is consistent with the slightly dispersed injection in the observations. The electron fluxes in the simulation show an increase which is different from the observations, partly because the satellite is close to the RCM dusk side tailward boundary and the westward electric field there draws particles at the boundary toward the Earth to 6.6 R_E. Since LANL89-046 is inside the injected bubble at the time of code onset, one would expect it to see dispersionless flux increases from both electrons and ions. LANL97A is outside the simulated bubble region, and it does not see the newly injected particles directly but sees them after the gradient and curvature drift around to the satellite; thus it observes dispersional proton injection. The injection picture we infer from the simulation is generally consistent with the analysis by *Liu et al.* [2009], except that we also see a dispersionless ion flux increase since our injection boundary is wider in local time compared to their conclusion. The dispersionless electron injection in our simulation has a ramp-up time in the order of ~10 min, while the injection in the observation is faster (a few minutes). That
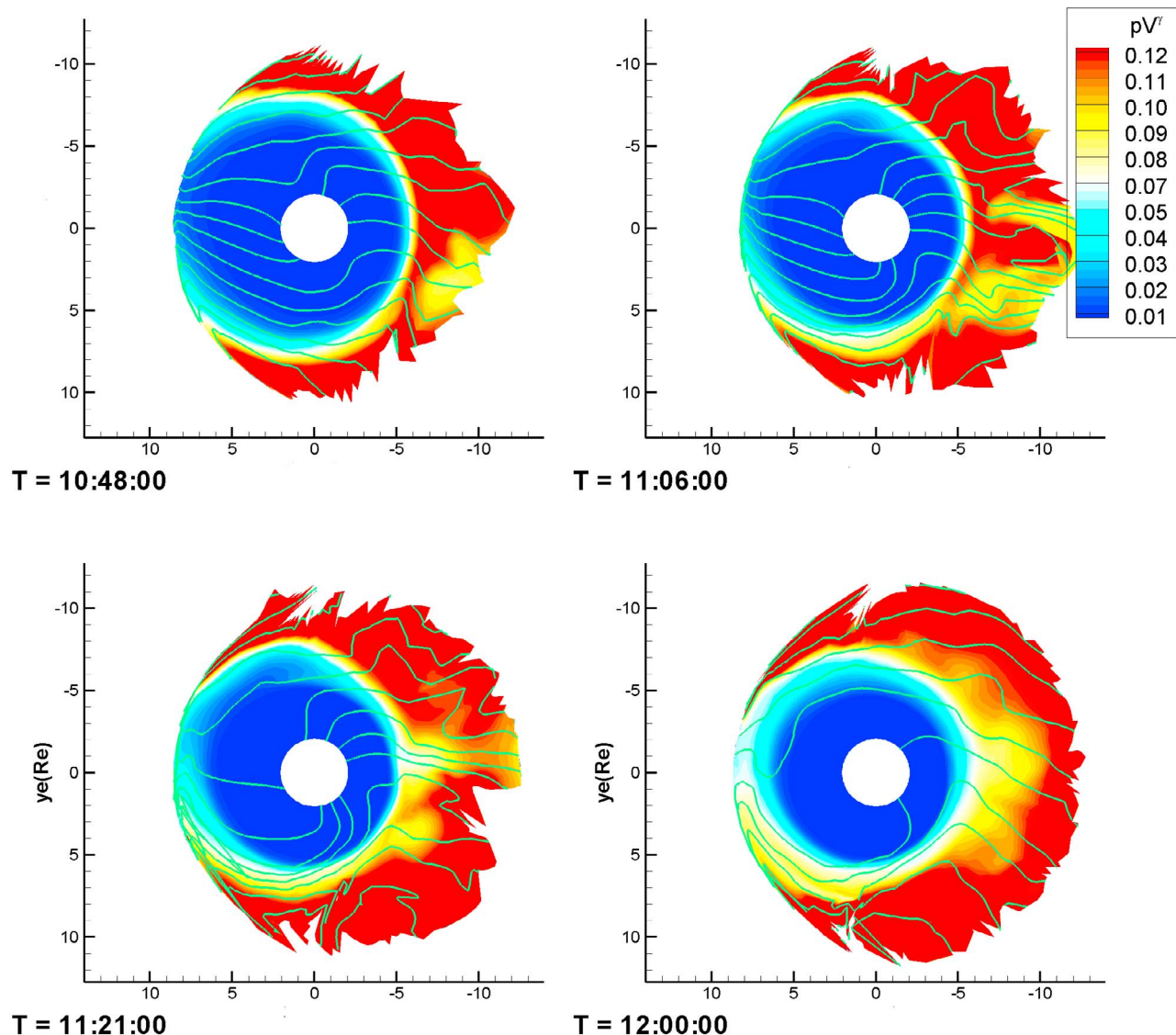
Figure 10. $PV^{5/3}$ time series plot of the bubble injection on the equatorial plane for the run using RCM potential solver (Run2). Solid lines are ionospheric potential with a spacing of 5 kV.

difference may be partially due to the fact that the earthward flow in the MHD is slower than what was observed. The observation at THEMIS C (closest to tail center at X ~ −7 R_E) indicates earthward flow as high as 300 km/s, while the MHD earthward flow velocity is ~100 km/s at ~−9 R_E around the code onset time (Figure 6).

[21] Figure 9 compares the simulation results from Run1 with the observed MPA moments, specifically the partial density and partial pressure in the energy range for the two LANL satellites. Figure 9 (left) shows the simulation results and Figure 9 (right) shows the observational data. LANL MPA instruments measure the charged particle distribution from 1 eV to ~40 keV, while the corresponding RCM quantity is obtained by summing the energy channels within the measurement range. The partial pressure for the measurement is calculated by summing the partial pressure for the high-energy protons (0.13–45 keV) and the pressure for the electrons. Though there are unfortunate gaps where observations were not available, overall, the simulation captures the trend

of the density and pressure variation. However, the RCM tends to overestimate the density. This is partly due to the higher density at the inner edge of the plasma sheet resulting from the boundary condition that was imposed on RCM before the dipolarization. In addition, the RCM pressure is higher than the observations and this and the higher densities may be due to the fact that the magnetic field is not responding to the RCM pressures, since feedback to the MHD code is not turned on. In simulations with self-consistent magnetic fields, the pressure in the inner magnetosphere tends to be lower than in simulations with non-self-consistent magnetic field [*Zaharia et al.*, 2005]. Pressure is lower in two-way coupled OpenGGCM/RCM runs than in the standalone RCM. These results do suggest the importance of a self-consistent magnetic field in matching observations.

[22] The overall reasonable agreement between simulation and data confirms the association of substorm injections with earthward moving bubbles. It also demonstrates that the OpenGGCM model, when coupled with the RCM, can be
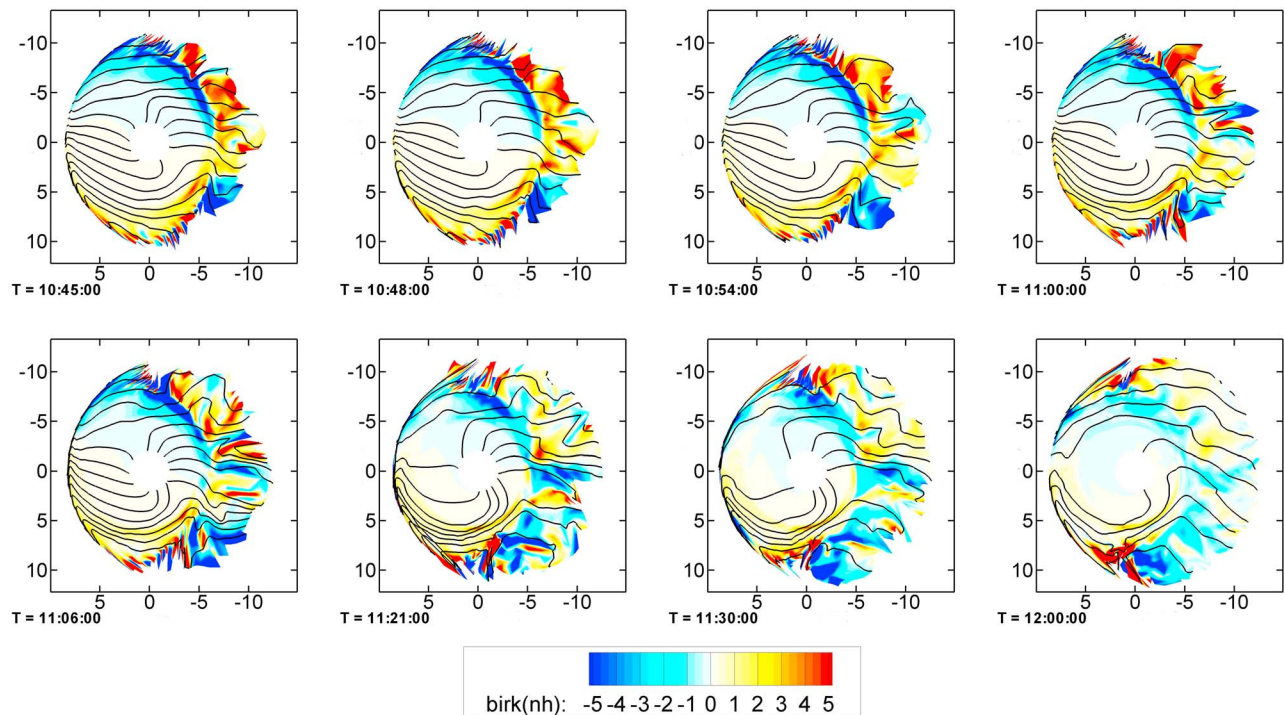
Figure 11. Birkeland currents in microamperes per square meter (color) and potential (contours) for the run using the RCM electric field (Run2). Positive Birkeland currents (yellow to red) are down into the ionosphere, while negative currents (blue) are up from the ionosphere. The current densities are ionospheric values mapped to the equatorial plane.

used to simulate substorm injection events, although feedback to the magnetic field could be important.

4. Results Using the RCM Computed Electric Field (RCM Run2)

4.1. Differences Between MHD- and RCM-Computed Electric Fields

[23] In this section, we present results from a run in which the potential electric field was computed using RCM rather than MHD machinery. There are several major differences in the procedure.

[24] 1. The two procedures calculate Birkeland currents in profoundly different ways. OpenGGCM calculates $\hat{b} \cdot \nabla \times \mathbf{B}$ on a spherical surface at ~4 R_E and then maps the currents to the Earth's surface assuming dipole field lines. The RCM uses a completely different approach, based on the current conservation equation written in the form

$$\frac{J_{\|i}}{B_i} = -\int \nabla \cdot \mathbf{J}_\perp \frac{ds}{B}. \qquad (4)$$

The two approaches are both based on MHD and are equivalent, in principle, provided that inertial currents are unimportant. However, the OpenGGCM usually do not have enough grid points near 4.5 R_E to resolve the complex auroral Birkeland currents.

[25] 2. The MHD code includes inertial currents in its calculation of $\mathbf{J}_\perp$, while the RCM neglects those currents entirely and assumes that $\mathbf{J}_\perp = \mathbf{B} \times \nabla P/B^2$. (Substituting this in (4) gives Vasyliunas equation $J_\| = \hat{b} \cdot \nabla V \times \nabla P/2$, after some manipulation.) The RCM's neglect of inertial currents constitutes a fundamental problem in using the code to treat fast moving bubbles. As noted in section 2.2, use of the RCM is usually limited to subsonic flow regions and precludes representation of waves. The run presented here that uses the MHD-calculated ionospheric potential includes inertial currents, but it has numerical difficulties, as described in items 1, 3, and 4. We are still working to find a procedure that includes the effects of inertial currents without the numerical problems inherent in the MHD code.

[26] 3. The MHD code sets Birkeland currents equal to zero for field lines with $L < {\sim}4$.

[27] 4. Figure 5 makes it clear that the RCM- and MHD-computed pressure distributions, which strongly affect the Birkeland currents, are very different. There are several reasons for this. First, the RCM initial condition includes a realistic trapped particle population near the Earth, while the MHD initial condition does not. Consequently, the RCM pressures are higher near the Earth. Second, the MHD code does not include transport by gradient/curvature drift, which is important in the inner plasma sheet and ring current. Third, there is much more numerical diffusion in the MHD code than in the RCM, and it tends to diffuse plasma outward from the high-pressure near-Earth region.

[28] In the two-way coupled case, MHD pressures are forced to be approximately consistent with RCM values, but that is not true in the present one-way coupled code used here. Considering all of the differences between the two approaches for computing $J_\|$, one might expect them to give
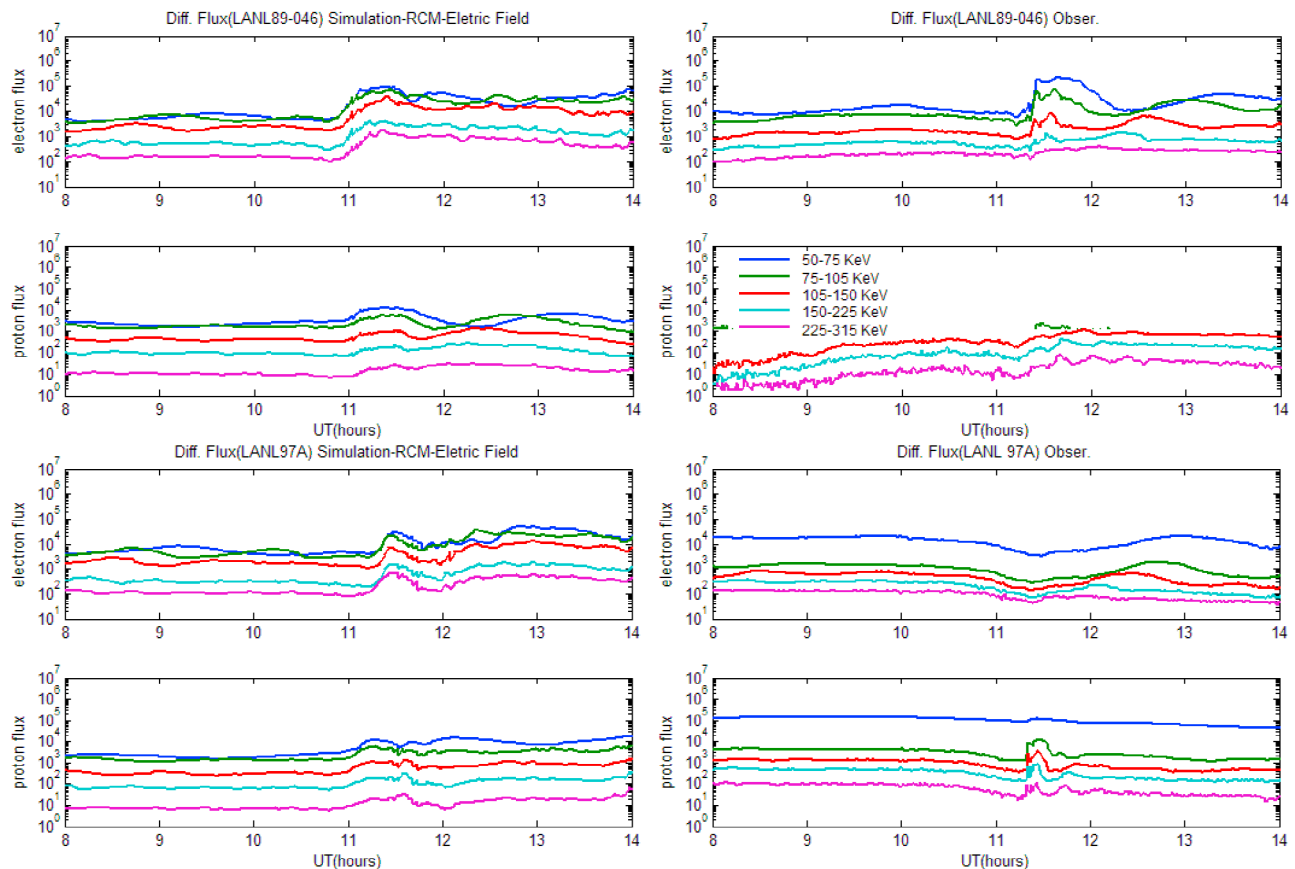
Figure 12. Simulation of SOPA fluxes versus observations for satellite LANL97A and LANL89-064, using the RCM electric field (Run2). The energies are 50–75, 75–105, 105–150, 150–225, and 225–315 keV, from blue to purple. The simulation results have been time-shifted 30 min.

different results, and they do. The MHD-computed Birkeland currents shown in Figure 5 are indeed very different from the RCM results.

[29] 5. Both codes use routines for solving $\nabla \cdot \Sigma \cdot \nabla \Phi = -j_{\parallel}$ sin I on a 2-D spherical grid; the RCM grid is denser than the OpenGGCM ionospheric grid but covers less latitude. The two have the same potential on the high-latitude boundary of the RCM, because the RCM takes its boundary condition there from MHD. However, the low-latitude boundary conditions for the potential solvers are different and are applied at different locations (45° latitude for RCM, 0° for MHD). Since the mapping originates from a spherical shell around the Earth at ~3.5 R_E, the MHD electric field solution below ~58° is artificial. The conductances are the same, as the OpenGGCM conductance model is used in both cases.

4.2. Bubble

[30] Figure 10 shows four snapshots of the entropy parameter $PV^{5/3}$ and the potential for the run using the RCM potential solver (Run2); it should be compared to results shown in Figures 4 for Run1, which used the MHD potentials. The bubble injection process in this run is quite similar in the two runs. For example, the low-$PV^{5/3}$ channel opens and closed at around the same times as in the run with OpenGGCM potential, which is due to the OpenGGCM magnetic field and plasma boundary conditions. Both runs

show enhanced westward electric field inside the bubble. However, the electric field in the bubble is stronger in the run using RCM potential and the bubbles travel slightly faster (e.g., by comparing plots at UT 11:21 and 12:00). The difference is probably due to a combination of factors 1, 2, and 4 in section 4.1. Figure 11 shows the mapped equatorial time series plots for the ionospheric Birkeland currents with potential contours. From the time series of the contours, the potential electric field increases in the bubble region during the injection and exhibits weak shielding near the Earth, although the region-2 Birkeland currents are well defined. The leading edge of the bubble caused a misalignment of the gradient of $PV^{5/3}$ and the gradient of the flux tube volume. Thus according to the Vasyliunas equation [*Wolf*, 1983] a wedge-like current is generated in the RCM around midnight. After the injection these currents become weaker. The two runs also give similar SOPA predictions; Figure 12 shows the geosynchronous SOPA fluxes for the case using RCM-computed electric field and they are very similar to the results using the OpenGGCM potential (Figure 8). Figure 13 compares observational data with model-computed plasma moments, for the run using the RCM electric field, and they are also similar to the results using the OpenGGCM potential (Figure 9) except that pressure and density values obtained in this run are closer to observations.
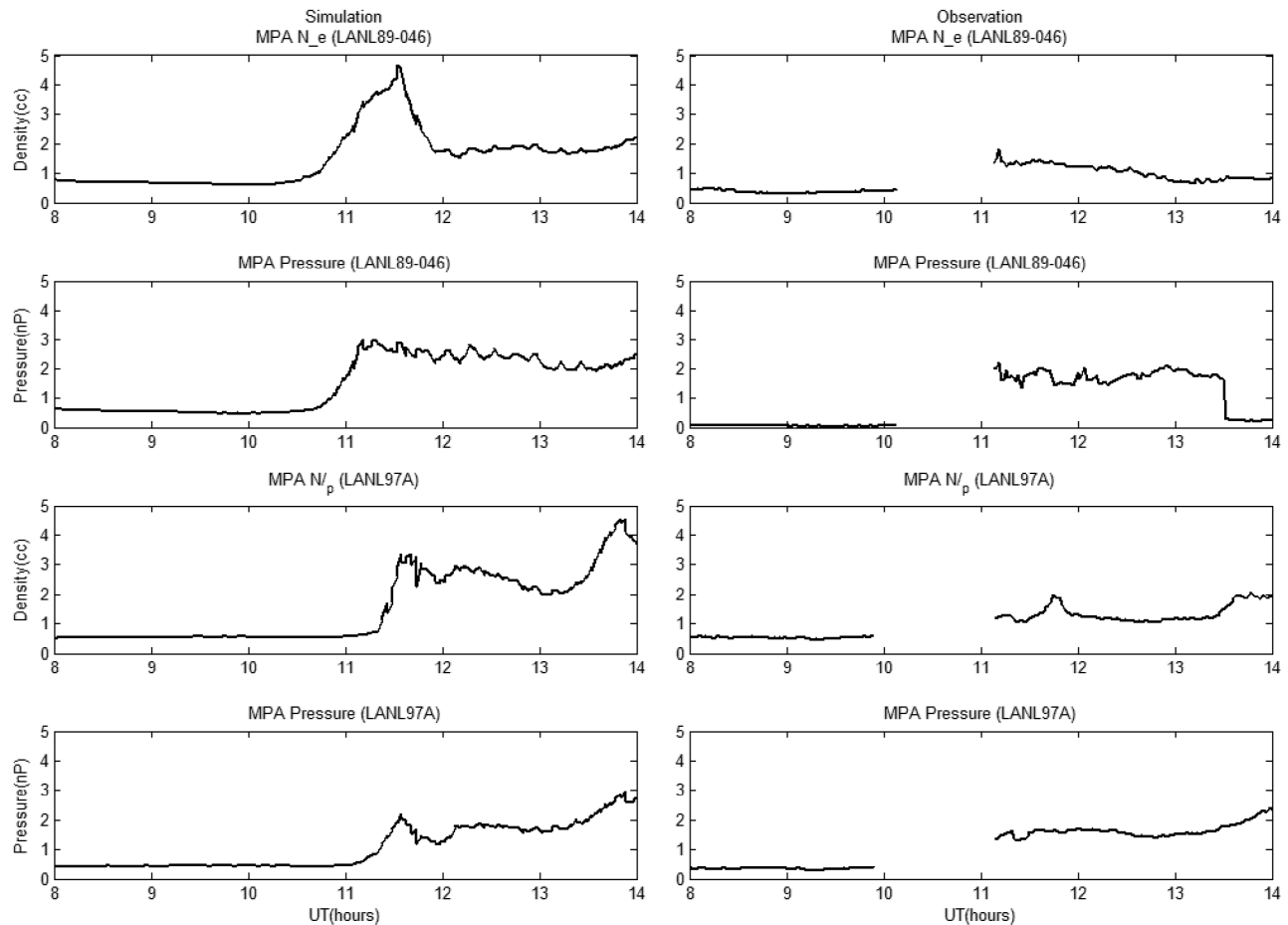
Figure 13. The same as Figure 8 but for the run using the RCM electric field (RCM Run2).

[31] The differences between the two electric fields are greatest in the near Earth region. The MHD-based potential from Run1 shown in Figure 4 exhibits little or no shielding in the inner magnetosphere while in the same region the RCM potential from Run2 in Figure 10 shows significant shielding of the cross tail potential. The weaker region-2 currents computed by the MHD may be due to the limited resolution for computing currents in the inner magnetosphere.

[32] The bubble injections are quite similar in the two runs, due to the fact that the bubbles were injected partly by the induction electric fields (same in both runs) and partly because the potential electric field in the bubble differs only moderately in the two runs. The RCM generally produces a more realistic electric field distribution, particularly because it exhibits significant shielding and other known features. Some implications of that difference will be explored in section 4.3.

4.3. Plasmasphere Plume After Bubble Injection

[33] The plasmasphere contains particles of mostly ionospheric origin with energy around 1 eV. The motion of these cold particles is determined by the electric field, including the effect of the Earth's rotation. The plasmasphere can have significant structure; such as the plasmaspheric plume, which is thought to form during enhanced magnetosphere convection [e.g., *Pierrard et al.*, 2009]. To simulate the plasmasphere in the RCM, we set the lowest-energy channel with

density values from *Gallagher et al.* [2000] model as an initial condition. This low-energy channel has a very low invariant energy so it carries a large density but an insignificant total pressure. This approach neglects the long-term effects such as refilling and night side losses, but the effects of these are limited due to the short runs.

[34] Figure 14 shows snapshots of the plasmaspheric density from Run2 for three times, one before the arrival of the bubbles, one during the bubble injection and one just after. The potential lines on these plots are ionospheric potential with corotation and thus are approximately the instantaneous drift paths for this low-energy channel, aside from the effects of induction electric fields, which are modest in the inner magnetosphere. Figure 15 shows the equatorial potential electric field comparison between Run1 (Figure 15a) and Run2 (Figure 15b). RCM Birkeland currents on the ionosphere in the run using RCM potential (Run2) and the OpenGGCM field-aligned currents on the ionosphere (Figure 15d) are also compared in Figure 15. The RCM electric field computed self-consistently with the plasma shows an enhanced electric field in the dusk and midnight sector (~5–6 R_E) after the bubble injection. These strong electric fields near the dusk side of the plasmapause, usually called SubAuroral Ionization Drift (SAID) events [*Spiro et al.*, 1979], cause particles in the plasmasphere to $\vec{E} \times \vec{B}$ drift westward and then sunward, and eventually creating a
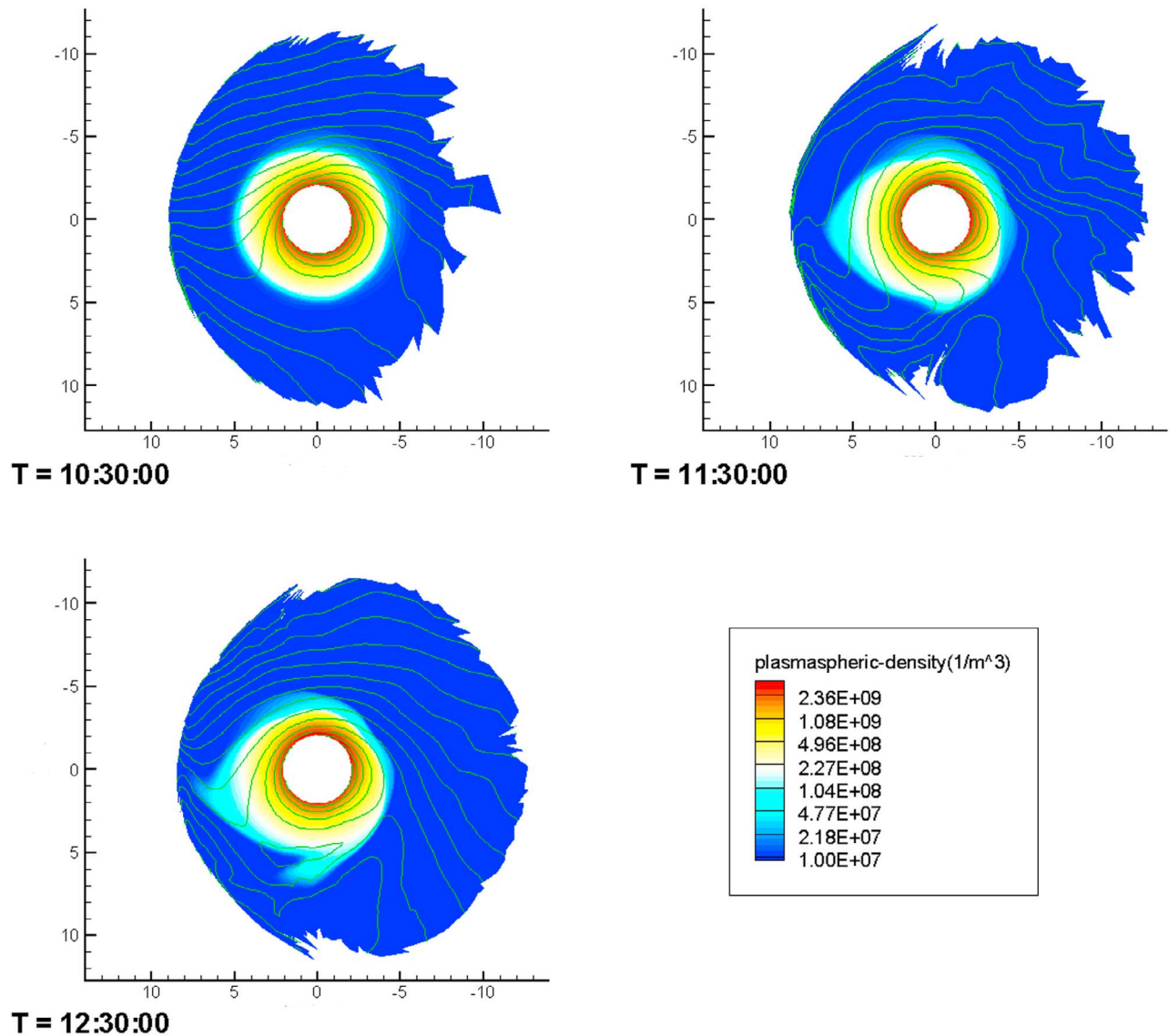
Figure 14. Plasmaspheric density on the equatorial plane before, during, and after the bubble injection for RCM Run2. Solid lines are the potential (including corotation).

plasmaspheric plume [*Goldstein et al.*, 2005]. The polar cap potential drop in the RCM modeling region decreases from ~80 kV to ~50 kV (shown in Figure 2) during the injection, and a shielding appears. If viewed on the ionosphere, the downward region-2 currents at the dusk-midnight sector move equatorward into the lower conductance region and thus strong electric field is produced [*Southwood and Wolf*, 1978]. Since the OpenGGCM does not resolve the Birkeland currents at this region, the electric field it obtains does not show this feature in the inner magnetosphere. There is a region near the Earth with strong electric field from OpenGGCM (Run1) after the onset as seen in Figure 15. Since this region is inside the OpenGGCM inner boundary, the strong electric field could be an artifact of the low conductance and the weak region-2 currents (shown in Figure 15). The spotty structures shown in OpenGGCM computed Birkeland currents, although are consistent with many observations [e.g., *Iijima and Potemra*, 1976; *Sitnov et al.*, 2010]

will be further investigated in future studies. Unfortunately there are no available observations at the event time to confirm the existence of a plasmaspheric plume in this event, but the results indicate the need to use RCM self-consistent electric field to more accurately model the inner magnetosphere electric field.

5. Discussion and Conclusions

[35] A one-way coupled OpenGGCM and RCM simulation was carried out to investigate a substorm event on 23 March 2007. It is the first time that a coupled MHD-RCM code has been used to simulate a substorm injection event, picturing the injection process in terms of earthward moving bubbles. In this simulation, the OpenGGCM magnetic field and plasma information are used as input and boundary conditions to the RCM, assuming the OpenGGCM provides reasonably good magnetic field, although feedback of the
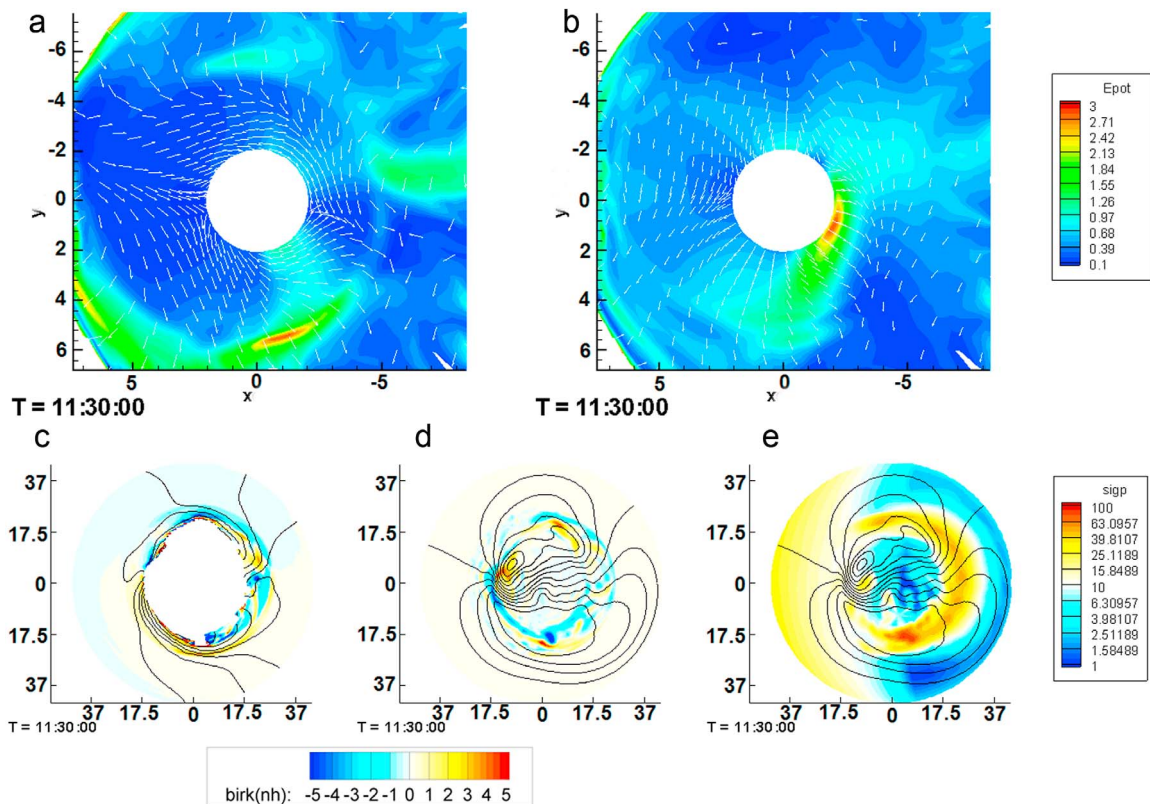
Figure 15. Equatorial potential electric field (mV/m) comparison between (a) the RCM potential from Run2 and (b) the OpenGGCM potential from Run1. Contours are electric field strength and the vectors show the direction. (c) RCM Birkeland currents ($\mu A/m^2$) from Run2 are shown in the ionosphere in solid lines with a spacing of 5 kV. (d) OpenGGCM field-aligned currents ($\mu A/m^2$) in the ionosphere with OpenGGCM computed potential in solid lines with a spacing of 5 kV. (e) The Pedersen conductance (S) in the ionosphere is shown with OpenGGCM computed potential. The Sun is to the left. All ionospheric parameters shown are for northern hemisphere.

RCM pressures and densities will likely change the magnetic field in the inner magnetosphere and have some impact on the results at geosynchronous orbit. In addition, a quiet time ring current model is used as the RCM initial condition. We found bubbles to be injected into the inner magnetosphere during the substorm expansion phase and the associated geosynchronous energetic particle injection. The bubble injection picture is consistent with other recent modeling work which uses different methods to drive the RCM. In the earlier simulations [e.g., *Yang et al.*, 2008; *Zhang et al.*, 2008, 2009], bubbles were produced by assuming low $PV^{5/3}$ on part or all of the RCM tailward boundary; in the present case, the bubbles were produced by the MHD calculation itself.

[36] To gain insight into how the MHD code created bubbles, we looked at the entropy parameter $PV^{5/3}$ in the OpenGGCM and found that the major injected bubbles were from magnetic reconnection in the MHD code. Multiple reconnection sites at different local times and distances were observed and their evolution through time was found to be complicated. There were signs of violation of ideal MHD before the code onset near ~11 R_E on the night side, probably because of numerical diffusion. The simulation indicates that in a real event, the bubble creation and propagation could be more complicated than the simplified 2-D picture. The MHD calculation suggests that the processes are much more com-

plex and dynamic than was represented by the simple ad hoc boundary conditions assumed in the earlier calculations [*Yang et al.*, 2008; *Zhang et al.*, 2008, 2009].

[37] We compare the RCM energetic particle flux with data measured by the SOPA and plasma moments with MPA data on LANL-97A and LANL-89-046 satellites. The simulation results are in general consistent with observation. In our simulation, a dispersionless injection is predicted at the virtual LANL-89-046 satellite and dispersed flux increase at the LANL-97A virtual satellite. The simulation showed a qualitatively reasonable picture of the bubble injection into the inner magnetosphere during a magnetospheric substorm.

[38] The simulation also demonstrated that by coupling an inner magnetosphere ring current model to a global MHD model, one can add missing physics to the MHD model, which cannot study processes like dispersed substorm particle injection on its own. The implication of the bubble injection found in this simulation is encouraging for the continuing development of MHD and RCM coupling, since it provides a consistent approach to nonadiabatic bubble creation and adiabatic bubble convection.

[39] A comparison simulation in which the electric field is self-consistently solved by RCM is also presented, confirming the injection picture and suggesting the need to use

RCM's electric field. The reasons why the two setups of runs gave similar bubble dynamics and fluxes are as follows.

[40] 1. The bubble injection is a short time scale process and the inner magnetosphere on a global scale might not have enough time to respond. Although the movement of the bubble has feedback to its local electric field, it is generally not sensitive to the ionospheric feedback of the region-2 currents in such short time scale. In particular, the more energetic particles are not sensitive to the electric field.

[41] 2. The motion of the bubble largely depends on the local magnetic field (the same in two runs) and electric field (similar in the bubble region). From Figure 5, we can see that the current structure in the bubble-injection region is similar in the RCM and OpenGGCM cases, although the MHD currents are more diffuse, and region-2 currents are weaker.

[42] 3. Before the injection, the IMF Bz is mostly northward and the convection strength is weak from 07:00 UT to 10:00 UT. When the IMF turns southward at ~10:00 UT, the polar cap potential starts to increase and region-2 currents start to build up. Since the RCM in Run2 use the OpenGGCM potential for its polar boundary condition, after a short time, the electric field from Run2 is similar to the electric field from Run1 at 10:45 UT except for the slightly better shielding. The similar preinjection electric field configuration contributes to the similar bubble dynamics of the two runs.

[43] Work toward a fully coupled RCM and OpenGGCM model will be continued to achieve better magnetospheric self-consistency. In these simulations, the pressure profiles computed by OpenGGCM and RCM differ considerably in the inner magnetosphere (e.g., the pressure profile comparison shown in Figure 5c). Although the timescale for a substorm event is much shorter than a storm, it may still be substantially impacted by the RCM feedback to the OpenGGCM, e.g., in the growth phase of the substorm. Future work will show how much impact the lack of pressure consistency between the RCM and the MHD has in terms of the detailed dynamics of a substorm.

[44] Another issue that arises with the use of RCM to simulate the fast moving bubbles is the possibility of violating the RCM slow-flow assumption. The neglect of inertial currents limits the RCM to work in subsonic flow regions and precludes representation of waves. The problem could be partially addressed by adding those currents into the Vasyliunas equation and evaluation of the effects is needed. We are working to address these issues and they will be left for future study.

Appendix A: Exchange Information Between RCM and OpenGGCM

[45] The OpenGGCM is a parallel code so that different parts of the computational domain are solved on different nodes; it uses the message passing interface (MPI) library to exchange of information between computational nodes, while the current version of the RCM is serial so that all calculations are done on a single node. In order to communicate information from the OpenGGCM to the RCM, conversions have to be done to allow information exchange. The RCM works on a 2-D ionosphere grid which usually has grid size around 200×100. The OpenGGCM provides the following quantities to RCM on the boundary: η_s, the flux tube content per unit magnetic flux for particles of invariant energy λ_s, V the flux

tube volume, and the mapping point on the equatorial plane and the magnetic field at the mapping point. The OpenGGCM has magnetic field information and plasma density ρ and pressure P (or temperature T) on its 3-D grid, in GSE coordinates. It thus traces from every grid point of the RCM ionospheric grid (in the northern hemisphere) to the southern ionosphere to get the x and y locations where the field lines cross the equatorial plane, and the magnitude of the magnetic field, here the equatorial crossing point is defined as the crossing point between the field and the center of the current sheet. During the trace procedure, we use a dipole magnetic field inside 4.5 R_E, the MHD magnetic field outside 6.5 R_E and a smooth combination of the two fields in between. Interpolation is done to map the MHD ionospheric potential onto the RCM grid. To get the flux tube content per unit magnetic flux η for a particular chemical species(electron and proton) and particular energy invariant, from the single fluid MHD number density n and temperature T, one first has to assume a temperature ratio between electrons and protons. We take the observational plasma sheet ion and electron temperature ratio as $T_i/T_e = 7.8$ [Baumjohann et al., 1989]. Then we need to assume a distribution function $f_s(\lambda)$ for each particle species; then flux tube content can be derived using the formula

$$\eta_s = \int_{\lambda_{\min}}^{\lambda_{\max}} \frac{2^{5/2}\pi}{m_s^{3/2}} f_s(\lambda)\sqrt{\lambda}\,d\lambda, \qquad (A1)$$

where $\lambda_{\max}$ and $\lambda_{\min}$ are the minimum and maximum invariant energy values of channel s.

[46] One choice for the distribution function $f_s(\lambda)$ is a Maxwellian

$$f_s(\lambda_s) = n\left(\frac{m_s}{2\pi k T_s}\right)^{3/2} e^{-\left(\lambda_s V^{-2/3}/kT\right)}, \qquad (A2)$$

where k is the Boltzmann constant, n is particle number density, T is T_i for ions and T_e for electrons, and s denotes to different energy channels for particular particle species. Integration gives the conversion formula for flux tube content as

$$\eta_s = nV\left\{erf(X_{\max}) - erf(X_{\min}) - \frac{2}{\sqrt{\pi}}\left[X_{\max}e^{-X_{\max}^2} - X_{\min}e^{-X_{\min}^2}\right]\right\}, \qquad (A3)$$

where $X = \sqrt{\frac{|\lambda|}{kTV^{2/3}}}$, $X_{\max}$ is the value of X when $\lambda = \lambda_{\max}$ and $erf(x)$ is the error function.

[47] One can also assume a kappa distribution function as

$$f_s(\lambda) = n\left(\frac{m}{2\pi bkT}\right)^{3/2} \frac{\Gamma(\kappa+1)}{\Gamma(\kappa-1/2)} \frac{1}{\left(1+\frac{\lambda V^{-2/3}}{bkT}\right)^{\kappa+1}}, \qquad (A4)$$

where b is $\kappa - \frac{1}{2}$ and the other factors are defined in the same way as in (A2). The integration gives

$$\eta_s = \frac{4nV}{\sqrt{\pi}} \frac{\Gamma(\kappa+1)}{\Gamma(\kappa-1/2)} \int_{X_{\min}}^{X_{\max}} \frac{x^2}{(1+x^2)^{\kappa+1}}\,dx$$

with $X = \sqrt{\frac{|\lambda|}{bkTV^{2/3}}}$. From RCM's multifluid information to MHD, one just needs to sum up all the energy channels and

the formulas are

$$n = \sum_s \frac{\eta_s}{V} \tag{A5}$$

and

$$P = \frac{2}{3} \sum_s \eta_s |\lambda_s| |V|^{-5/3}. \tag{A6}$$

[49] Masaki Fujimoto thanks the reviewers for their assistance in evaluating this manuscript.

References

Angelopoulos, V., C. F. Kennel, F. V. Coroniti, R. Pellat, M. G. Kivelson, R. J. Walker, C. T. Russell, W. Baumjohann, W. C. Feldman, and J. T. Gosling (1994), Statistical characteristics of bursty bulk flow events, *J. Geophys. Res.*, 99, 21,257–21,280, doi:10.1029/94JA01263.

Angelopoulos, V., et al. (2008), First results from the THEMIS mission, *Space Sci. Rev.*, 141, 453–476, doi:10.1007/s11214-008-9378-4.

Apatenkov, S. V., et al. (2007), Multi-spacecraft observation of plasma dipolarization/injection in the inner magnetosphere, *Ann. Geophys.*, 25, 801–814, doi:10.5194/angeo-25-801-2007.

Baumjohann, W., G. Paschmann, and C. Cattell (1989), Average plasma properties in the central plasma sheet, *J. Geophys. Res.*, 94(A6), 6597–6606, doi:10.1029/JA094iA06p06597.

Belian, R. D., D. N. Baker, P. R. Higbie, and E. W. Hones Jr. (1978), High-resolution energetic particle measurements at 6.6 R_E, 2, high-energy proton drift echoes, *J. Geophys. Res.*, 83(A10), 4857–4862, doi:10.1029/JA083iA10p04857.

Birn, J., M. F. Thomsen, J. E. Borovsky, G. D. Reeves, D. J. McComas, R. D. Belian, and M. Hesse (1997), Substorm ion injections: Geosynchronous observations and test particle orbits in three-dimensional dynamic MHD fields, *J. Geophys. Res.*, 102(A2), 2325–2341, doi:10.1029/96JA03032.

Birn, J., M. F. Thomsen, J. E. Borovsky, G. D. Reeves, D. J. McComas, R. D. Belian, and M. Hesse (1998), Substorm electron injections: Geosynchronous observations and test particle simulations, *J. Geophys. Res.*, 103(A5), 9235–9248, doi:10.1029/97JA02635.

Birn, J., J. Raeder, Y. L. Wang, R. A. Wolf, and M. Hesse (2004), On the propagation of bubbles in the geomagnetic tail, *Ann. Geophys.*, 22(5), 1773–1786, doi:10.5194/angeo-22-1773-2004.

Birn, J., M. Hesse, and K. Schindler (2006), Entropy conservation in simulations of magnetic reconnection, *Phys. Plasmas*, 13, 092117, doi:10.1063/1.2349440.

Buzulukova, N., M.-C. Fok, A. Pulkkinen, M. Kuznetsova, T. E. Moore, A. Glocer, P. C. Brandt, G. Toth, and L. Rastaetter (2010), Dynamics of ring current and electric fields in the inner magnetosphere during disturbed periods: CRCM–BATS-R-US coupled model, *J. Geophys. Res.*, 115, A05210, doi:10.1029/2009JA014621.

Christon, S. P., D. G. Mitchell, D. J. Williams, L. A. Frank, C. Y. Huang, and T. E. Eastman (1988), Energy spectra of plasma sheet ions and electrons from ~50 eV/e to ~1 MeV during plasma temperature transitions, *J. Geophys. Res.*, 93(A4), 2562–2572, doi:10.1029/JA093iA04p02562.

De Zeeuw, D. L., S. Sazykin, R. A. Wolf, T. I. Gombosi, A. J. Ridley, and G. Toth (2004), Coupling of a global MHD code and an inner magnetospheric model: Initial results, *J. Geophys. Res.*, 109, A12219, doi:10.1029/2003JA010366.

Evans, C. R., and J. F. Hawley (1988), Simulation of magnetohydrodynamic flows: A constrained transport method, *Astrophys. J.*, 332, 659–677, doi:10.1086/166684.

Fok, M.-C., T. E. Moore, and D. C. Delcourt (1999), Modeling of inner plasma sheet and ring current during substorms, *J. Geophys. Res.*, 104, 14,557–14,569, doi:10.1029/1999JA900014.

Fok, M.-C., R. A. Wolf, R. W. Spiro, and T. E. Moore (2001), Comprehensive computational model of Earth's ring current, *J. Geophys. Res.*, 106(A5), 8417–8424, doi:10.1029/2000JA000235.

Fok, M.-C., T. E. Moore, P. C. Brandt, D. C. Delcourt, S. P. Slinker, and J. A. Fedder (2006), Impulsive enhancements of oxygen ions during substorms, *J. Geophys. Res.*, 111, A10222, doi:10.1029/2006JA011839.

Fuller-Rowell, T. J., D. Rees, S. Quegan, R. J. Moffett, M. V. Codrescu, and G. H. Millward (1996), A coupled thermosphere-ionosphere model (CTIM), in *STEP Handbook on Ionospheric Models*, edited by R. W. Schunk, pp. 217–238, Utah State Univ., Logan.

Gallagher, D. L., P. D. Craven, and R. H. Comfort (2000), Global core plasma model, *J. Geophys. Res.*, 105(A8), 18,819–18,833, doi:10.1029/1999JA000241.

Goldstein, J., J. L. Burch, and B. R. Sandel (2005), Magnetospheric model of subauroral polarization stream, *J. Geophys. Res.*, 110, A09222, doi:10.1029/2005JA011135.

Harel, M., R. Wolf, P. Reiff, R. Spiro, W. Burke, F. Rich, and M. Smiddy (1981), Quantitative simulation of a magnetospheric substorm: 1. Model logic and overview, *J. Geophys. Res.*, 86(A4), 2217–2241, doi:10.1029/JA086iA04p02217.

Iijima, T., and T. A. Potemra (1976), The amplitude distribution of field-aligned currents at northern high latitudes observed by Triad, *J. Geophys. Res.*, 81(13), 2165–2174, doi:10.1029/JA081i013p02165.

Jaggi, R., and R. Wolf (1973), Self-consistent calculation of the motion of a sheet of ions in the magnetosphere, *J. Geophys. Res.*, 78(16), 2852–2866, doi:10.1029/JA078i016p02852.

Jordanova, V., L. Kistler, C. Farrugia, and R. Torbert (2001), Effects of inner magnetospheric convection on ring current dynamics: March 10–12, 1998, *J. Geophys. Res.*, 106(A12), 29,705–29,720, doi:10.1029/2001JA000047.

Keiling, A., et al. (2008a), Correlation of substorm injections, auroral modulations, and ground Pi2, *Geophys. Res. Lett.*, 35, L17S22, doi:10.1029/2008GL033969.

Keiling, A., et al. (2008b), Multiple intensifications inside the auroral bulge and their association with plasma sheet activities, *J. Geophys. Res.*, 113, A12216, doi:10.1029/2008JA013383.

Lemon, C., R. A. Wolf, T. W. Hill, S. Sazykin, R. W. Spiro, F. R. Toffoletto, J. Birn, and M. Hesse (2004), Magnetic storm ring current injection modeled with the Rice Convection Model and a self-consistent magnetic field, *Geophys. Res. Lett.*, 31, L21801, doi:10.1029/2004GL020914.

Li, X., D. N. Baker, M. Temerin, G. D. Reeves, and R. D. Belian (1998), Simulation of dispersionless injections and drift echoes of energetic electrons associated with substorms, *Geophys. Res. Lett.*, 25(20), 3763–3766, doi:10.1029/1998GL900001.

Li, X., T. E. Sarris, D. N. Baker, W. K. Peterson, and H. J. Singer (2003), Simulation of energetic particle injections associated with a substorm on August 27, 2001, *Geophys. Res. Lett.*, 30(1), 1004, doi:10.1029/2002GL015967.

Liemohn, M. W., J. U. Kozyra, V. K. Jordanova, G. V. Khazanov, M. F. Thomsen, and T. E. Cayton (1999), Analysis of early phase ring current recovery mechanisms during geomagnetic storms, *Geophys. Res. Lett.*, 26(18), 2845–2848, doi:10.1029/1999GL900611.

Lui, A. T. Y., R. E. Lopez, B. J. Anderson, K. Takahashi, L. J. Zanetti, R. W. McEntire, T. A. Potemra, D. M. Klumpar, E. M. Greene, and R. Strangeway (1992), Current disruptions in the near-Earth neutral sheet region, *J. Geophys. Res.*, 97(A2), 1461–1480, doi:10.1029/91JA02401.

Liu, W. L., X. Li, T. Sarris, C. Cully, R. Ergun, V. Angelopoulos, D. Larson, A. Keiling, K. H. Glassmeier, and H. U. Auster (2009), Observation and modeling of the injection observed by THEMIS and LANL satellites during the 23 March 2007 substorm event, *J. Geophys. Res.*, 114, A00C18, doi:10.1029/2008JA013498.

Lyon, J. G., J. A. Fedder, and C. M. Mobarry (2004), The Lyon-Fedder-Mobarry (LFM) global MHD magnetospheric simulation code, *J. Atmos. Sol. Terr. Phys.*, 66, 1333–1350, doi:10.1016/j.jastp.2004.03.020.

Lyons, L. R., C.-P. Wang, T. Nagai, T. Mukai, Y. Saito, and J. C. Samson (2003), Substorm inner plasma sheet particle reduction, *J. Geophys. Res.*, 108(A12), 1426, doi:10.1029/2003JA010177.

Mauk, B. H., and C.-I. Meng (1987), Plasma injection during substorms, *Phys. Scr.*, T18, 128–139, doi:10.1088/0031-8949/1987/T18/014.

Moore, T. E., M.-C. Fok, D. C. Delcourt, S. P. Slinker, and J. A. Fedder (2008), Plasma plume circulation and impact in an MHD substorm, *J. Geophys. Res.*, 113, A06219, doi:10.1029/2008JA013050.

Pierrard, V., J. Goldstein, N. André, V. K. Jordanova, G. A. Kotova, J. F. Lemaire, M. W. Liemohn, and H. Matsui (2009), Recent progress in physics-based models of the plasmasphere, *Space Sci. Rev.*, 145, 193–229, doi:10.1007/s11214-008-9480-7.

Pontius, D. H., Jr., and R. A. Wolf (1990), Transient flux tubes in the terrestrial magnetosphere, *Geophys. Res. Lett.*, 17, 49–52, doi:10.1029/GL017i001p00049.

Powell, K. G., P. L. Roe, T. J. Linde, T. I. Gombosi, and D. L. De Zeeuw (1999), A solution-adaptive upwind scheme for ideal magnetohydrodynamics, *J. Comput. Phys.*, *154*, 284–309, doi:10.1006/jcph.1999.6299.

Raeder, J. (2003), Global magnetohydrodynamics—A tutorial, in *Space Plasma Simulation*, *Lecture Notes Phys.*, vol. 615, edited by J. Buechner, C. T. Dum, and M. Scholer, Springer, Berlin.

Raeder, J., J. Berchem, and M. Ashour-Abdalla (1998), The Geospace Environment Modeling Grand Challenge: Results from a Global Geospace Circulation Model, *J. Geophys. Res.*, *103*(A7), 14,787–14,797, doi:10.1029/98JA00014.

Raeder, J., R. L. McPherron, L. A. Frank, S. Kokubun, G. Lu, T. Mukai, W. R. Paterson, J. B. Sigwarth, H. J. Singer, and J. A. Slavin (2001), Global simulation of the Geospace Environment Modeling substorm challenge event, *J. Geophys. Res.*, *106*, 381, doi:10.1029/2000JA000605.

Raeder, J., J. Dorelli, D. Larson, and B. Loring (2006), Physical, numerical, and computational challenges in modeling the geospace environment, *Astron. Soc. Pac. Conf. Ser.*, *359*, 202.

Raeder, J., D. Larson, W. Li, E. L. Kepko, and T. Fuller-Rowell (2008), OpenGGCM simulations for the THEMIS mission, *Space Sci. Rev.*, *141*, 535–555, doi:10.1007/s11214-008-9421-5.

Sergeev, V., V. Angelopoulos, J. Gosling, C. Cattell, and C. Russell (1996), Detection of localized, plasma-depleted flux tubes or bubbles in the midtail plasma sheet, *J. Geophys. Res.*, *101*, 10,817–10,826, doi:10.1029/96JA00460.

Sitnov, M. I., P. N. Guzdar, and M. Swisdak (2007), Atypical current sheets and plasma bubbles: A self-consistent kinetic model, *Geophys. Res. Lett.*, *34*, L15101, doi:10.1029/2007GL029693.

Sitnov, M. I., N. A. Tsyganenko, A. Y. Ukhorskiy, B. J. Anderson, H. Korth, A. T. Y. Lui, and P. C. Brandt (2010), Empirical modeling of a CIR-driven magnetic storm, *J. Geophys. Res.*, *115*, A07231, doi:10.1029/2009JA015169.

Southwood, D. J., and R. A. Wolf (1978), An assessment of the role of precipitation in magnetospheric convection, *J. Geophys. Res.*, *83*(A11), 5227–5232, doi:10.1029/JA083iA11p05227.

Spence, H. E., and M. G. Kivelson (1993), Contributions of the low-latitude boundary layer to the finite width magnetotail convection model, *J. Geophys. Res.*, *98*(A9), 15,487–15,496, doi:10.1029/93JA01531.

Spiro, R. W., R. A. Heelis, and W. B. Hanson (1979), Rapid subauroral ion drifts observed by Atmosphere Explorer C, *Geophys. Res. Lett.*, *6*(8), 657–660, doi:10.1029/GL006i008p00657.

Spiro, R. W., R. A. Wolf, and B. G. Fejer (1988), Penetration of high-latitude-electric-field effects to low latitudes during SUNDIAL 1984, *Ann. Geophys.*, *6*, 39–50.

Taktakishvili, A., M. Kuznetsova, M. Hesse, L. Rastatter, A. Chulaki, and A. Pulkkinnen (2007), Metrics analysis of the coupled Block Adaptive-Tree Solar Wind Roe-Type Upwind Scheme and Fork ring current model performance, *Space Weather*, *5*, S11004, doi:10.1029/2007SW000321.

Thomsen, M. F., J. Birn, J. E. Borovsky, K. Morzinski, D. J. McComas, and G. D. Reeves (2001), Two-satellite observations of substorm injections at geosynchronous orbit, *J. Geophys. Res.*, *106*(A5), 8405–8416, doi:10.1029/2000JA000080.

Toffoletto, F., S. Sazykin, R. W. Spiro, and R. A. Wolf (2003), Inner magnetosphere modeling with the Rice Convection Model, *Space Sci. Rev.*, *107*, 175–196, doi:10.1023/A:1025532008047.

Toffoletto, F., S. Sazykin, R. W. Spiro, R. A. Wolf, and J. G. Lyon (2004), RCM meets LFM: Initial results of on-way coupling, *J. Atmos. Terr. Phys.*, *66*, 1361–1370, doi:10.1016/j.jastp.2004.03.022.

Tóth, G., et al. (2005), Space Weather Modeling Framework: A new tool for the space science community, *J. Geophys. Res.*, *110*, A12226, doi:10.1029/2005JA011126.

Tóth, G., D. L. De Zeeuw, T. I. Gombosi, W. B. Manchester, A. J. Ridley, I. V. Sokolov, and I. I. Roussev (2007), Sun-to-thermosphere simulation of the 28–30 October 2003 storm with the Space Weather Modeling Framework, *Space Weather*, *5*, S06003, doi:10.1029/2006SW000272.

Vasyliunas, V. M. (1970), Mathematical models of magnetospheric convection and its coupling to the ionosphere, in *Particles and Fields in the Magnetosphere*, edited by B. M. McCormac, pp. 60–71, D. Reidel, Hingham, Mass.

Walsh, A. P., et al. (2009), Cluster and Double Star multipoint observations of a plasma bubble, *Ann. Geophys.*, *27*, 725–743, doi:10.5194/angeo-27-725-2009.

Wolf, R. A. (1970), Effects of ionospheric conductivity on convective flow of plasma in the magnetosphere, *J. Geophys. Res.*, *75*(25), 4677–4698, doi:10.1029/JA075i025p04677.

Wolf, R. A. (1983), The quasi-static (slow-flow) region of the magnetosphere, in *Solar-Terrestrial Physics*, edited by R. L. Carovillano and J. M. Forbes, pp. 303–368, D. Reidel, Hingham, Mass.

Wolf, R. A., Y. Wan, X. Xing, J.-C. Zhang, and S. Sazykin (2009), Entropy and plasma sheet transport, *J. Geophys. Res.*, *114*, A00D05, doi:10.1029/2009JA014044.

Yang, J., F. R. Toffoletto, R. A. Wolf, S. Sazykin, R. W. Spiro, P. C. Brandt, M. G. Henderson, and H. U. Frey (2008), Rice convection Model simulation of the 18 April 2002 sawtooth event and evidence for interchange instability, *J. Geophys. Res.*, *113*, A11214, doi:10.1029/2008JA013635.

Zaharia, S., C. Z. Cheng, and J. R. Johnson (2000), Particle transport and energization associated with substorms, *J. Geophys. Res.*, *105*(A8), 18,741–18,752, doi:10.1029/1999JA000407.

Zaharia, S., J. Birn, R. H. W. Friedel, G. D. Reeves, M. F. Thomsen, and C. Z. Cheng (2004), Substorm injection modeling with nondipolar, time-dependent background field, *J. Geophys. Res.*, *109*, A10211, doi:10.1029/2004JA010464.

Zaharia, S., J. Birn, and C. Z. Cheng (2005), Toward a global magnetospheric equilibrium model, *J. Geophys. Res.*, *110*, A09228, doi:10.1029/2005JA011101.

Zhang, J., et al. (2007), Understanding storm-time ring current development through data-model comparisons of a moderate storm, *J. Geophys. Res.*, *112*, A04208, doi:10.1029/2006JA011846.

Zhang, J.-C., R. A. Wolf, S. Sazykin, and F. R. Toffoletto (2008), Injection of a bubble into the inner magnetosphere, *Geophys. Res. Lett.*, *35*, L02110, doi:10.1029/2007GL032048.

Zhang, J.-C., R. A. Wolf, G. M. Erickson, R. W. Spiro, F. R. Toffoletto, and J. Yang (2009), Rice Convection Model simulation of the injection of an observed bubble into the inner magnetosphere: 1. Magnetic-field and other inputs, *J. Geophys. Res.*, *114*, A08218, doi:10.1029/2009JA014130.

Zhu, P., J. Raeder, K. Germaschewski, and C. C. Hegna (2009), Initiation of ballooning instability in the near-Earth plasma sheet prior to the 23 March 2007 THEMIS substorm expansion onset, *Ann. Geophys.*, *27*, 1129–1138, doi:10.5194/angeo-27-1129-2009.

B. Hu, S. Sazykin, F. R. Toffoletto, and R. A. Wolf, Department of Physics and Astronomy, Rice University, 6100 Main St., MS 108, Houston, TX 77005, USA. (bh1@rice.edu)

D. Larson, J. Raeder, and A. Vapirev, Space Science Center, University of New Hampshire, 8 College Rd., Durham, NH 03824, USA.